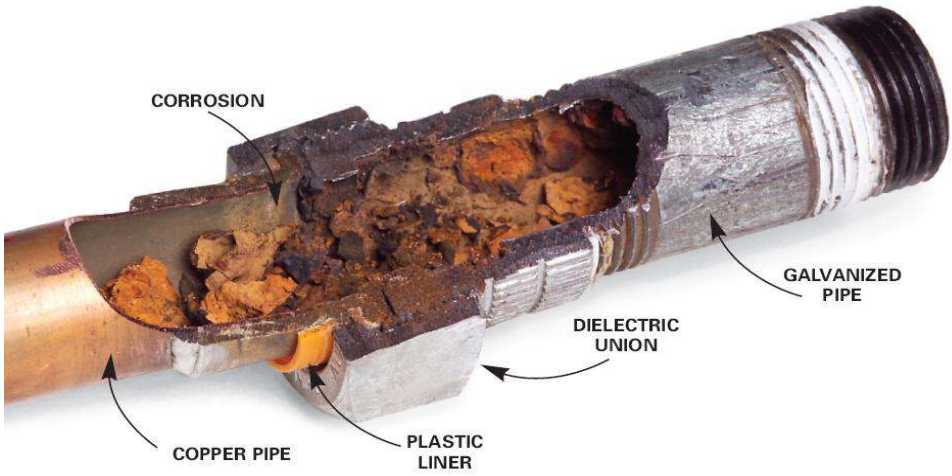

Chapter 9

Corrosion Behavior of Fe-Al_2O_3 Metal Matrix Nanocomposites

Chapter 9
Corrosion Behavior of Fe-Al_2O_3 Metal Matrix Nanocomposites

The present chapter describes the corrosion behavior of 5%, 10% Al_2O_3 reinforced and CoO and CeO_2 doped 10% Al_2O_3 reinforced Fe metal matrix nanocomposites. Corrosion behavior of the synthesized nanocomposite specimens was studied in 1 Normal HCl solution by using the Tafel polarization plots. XRD and SEM of the corroded specimens were also recorded in order to study the phase as well as morphology of respective surfaces. EDAX studies of CoO doped Fe-Al_2O_3 composite specimens were also made to verify the results of XRD. For comparison purpose and determination of anti-corrosive efficiency of different specimen, pure iron, CoO and CeO_2 doped pure iron specimens were prepared by P/M process and were characterized for their corrosion behavior.

9.1 Corrosion Behavior of 5% Al_2O_3 reinforcement

Iron - alumina based MMNC specimens, having composition 95wt% Fe (electrolytic grade with 99.5% purity; 250-300 mesh (49-58 μm)) and 5wt% Al_2O_3 (active; particle size of 70-230 mesh (63-210 μm)) were prepared using powder metallurgy technique. Green compacts, pressed at 7 tons were sintered in an argon atmosphere in the temperature range of 900 - 1100°C for 1 to 3 hours. A nomenclature e.g. 5AFe1100(2) of different specimens is given indicating sintering temperature and time as described in Chapter 5.

9.1.1 Tafel Polarization and Corrosion Behavior

Tafel polarization plots of all the 9 specimens sintered at 900, 1000 and 1100°C for 1, 2 and 3 hour were recorded. The values of corrosion potential (E_{corr}), corrosion current density (I_{corr}), were evaluated from the anodic and cathodic regions of Tafel

plots. The linear segments of anodic and cathodic curves were extrapolated to corrosion potential to obtain corrosion current densities (I_{corr}). Anti-corrosive efficiency (μ_p %) was evaluated from the measured I_{corr} values using the relationship:

$$\mu_p\ \% = (I^o_{corr} - I^i_{corr}) / I^o_{corr} * 100$$

where I^o_{corr} and I^i_{corr} are values of corrosion current density for pure iron and for specimens with aluminium oxide as reinforcement respectively.

Fig. 9.1 shows Tafel plots of specimens 5AFe900(1), 5AFe1000(1) and 5AFe1100(1) in 1N HCl solution. The figure indicates the dependence of corrosion resistance on the sintering temperature with fixed sintering time (1h) of the specimens. Tafel plots of the specimens 5AFe1100(1), 5AFe1100(2) and 5AFe1100(3) are shown in Fig. 9.2 in 1N HCl. This figure indicates the dependence of corrosion resistance on the sintering time with fixed sintering temperature (1100°C) of the specimens.

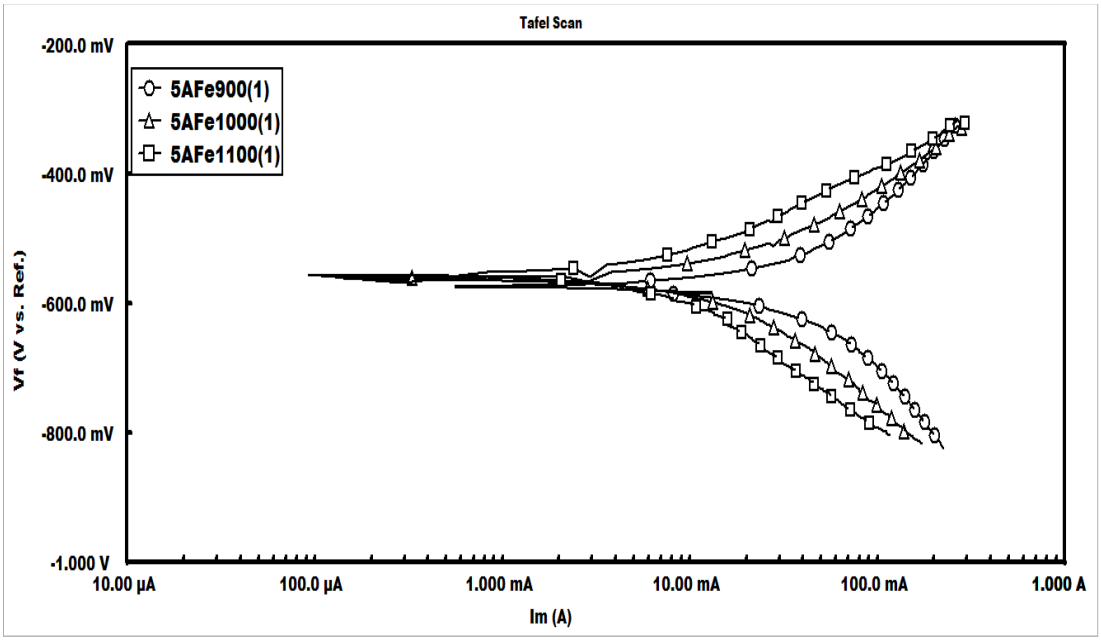

Fig. 9.1 Tafel plots of the specimens 5AFe900(1), 5AFe1000(1) and 5AFe1100(1) sintered for 1h at different temperatures

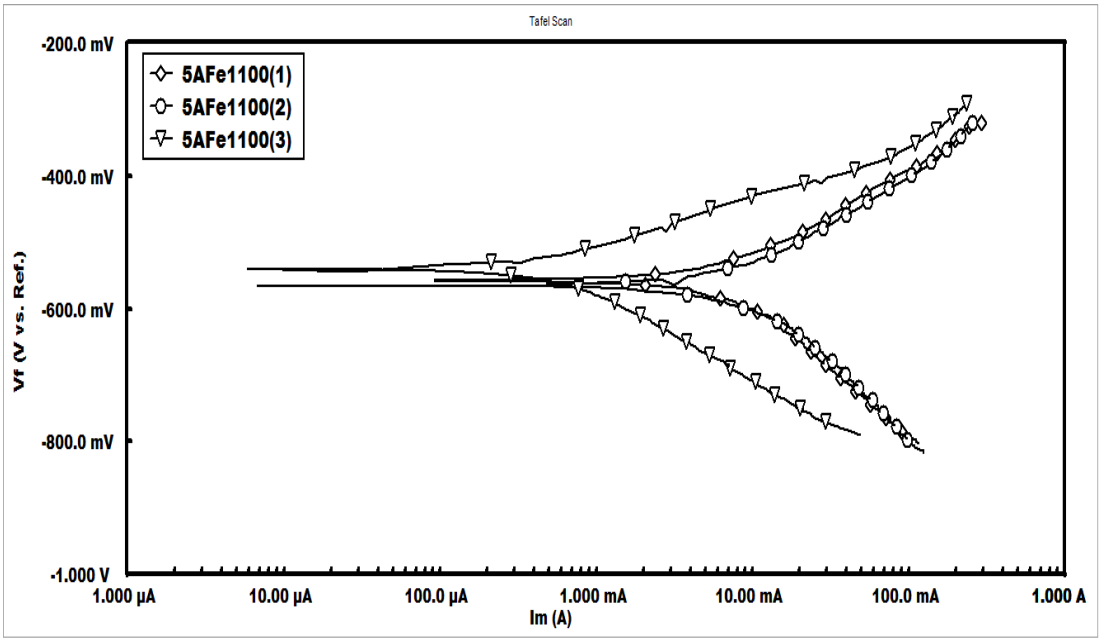

Fig. 9.2 Tafel plots of the specimens 5AFe1100(1), 5AFe1100(2) and 5AFe1100(3) sintered at same temperature for different times of sintering

Table 9.1 shows the E_{corr}, corrosion rate, I_{corr} and anti-corrosive efficiency (μ_p) values for the various specimens ranging from 5AFe900(1) to 5AFe1100(3) and a pure iron specimen respectively. It is observed that among the various synthesized specimens, the corrosion potential varied in the range -535 to -575 mV. Pure iron specimen shows highest corrosion rate of 92080 mpy and highest corrosion current of 200000 µA as compared to the specimens obtained using Al_2O_3 as the reinforcement. These values are very large in comparison to the values of all the nanocomposite specimens. Within the experimental limit, it was found that the specimen 5AFe1000(3) showed lowest anti-corrosion efficiency and highest corrosion current. The specimen 5AFe1100(1) and 5AFe1100(3) showed high anti-corrosion efficiency and low corrosion current as shown in Table 9.1. Variation of corrosion rate with respect to sintering temperature and time is shown in Fig. 9.3 and 9.4 respectively.

Table 9.1 E_{corr}, corrosion rate, I_{corr} and anti-corrosive efficiency (μ_p) values for the various 5% Al_2O_3 reinforced specimens

Sl. No.	Sample Code	E_{corr} (mV)	I_{corr} (µA)	Corrosion rate (mpy)	μ_p (%)
1.	5AFe900(1)	-572	14400	6647	92.78
2.	5AFe900(2)	-549	2270	1045	98.86
3.	5AFe900(3)	-573	8090	3730	95.94
4.	5AFe1000(1)	-561	4390	2023	97.80
5.	5AFe1000(2)	-559	13900	6419	93.02
6.	5AFe1000(3)	-570	21800	10040	89.09
7.	5AFe1100(1)	-555	173	79.94	99.91
8.	5AFe1100(2)	-565	9260	4267	95.36
9.	5AFe1100(3)	-539	70	32.35	99.96
10.	Pure iron	-559	200000	92080	-

Fig. 9.3 shows the variation of corrosion rate with sintering temperatures for different sintering time whereas Fig. 9.4 represents the variation of corrosion rate with sintering time for different sintering temperatures. From these figures and table 9.1 we observe that the corrosion rate was highest for the specimen 5AFe900(1) among the specimens sintered for 1h. For the specimen sintered for 2 hours the corrosion rate was highest for the specimen 5AFe1000(2), followed by 5AFe1100(2) and lastly for 5AFe900(2). Similarly the corrosion rate was highest for the specimen 5AFe1000(3) for the specimens sintered for 3h. The specimen 5AFe900(1) shows the highest corrosion followed by 5AFe1000(1) and then 5AFe1100(1). Specimen 5AFe900(2) showed the lowest corrosion rate among the specimens sintered for 2 hours. The corrosion rate was highest for 5AFe1000(3) followed by 5AFe900(3) and then 5AFe1100(3) for specimens sintered for 3h at different temperature.

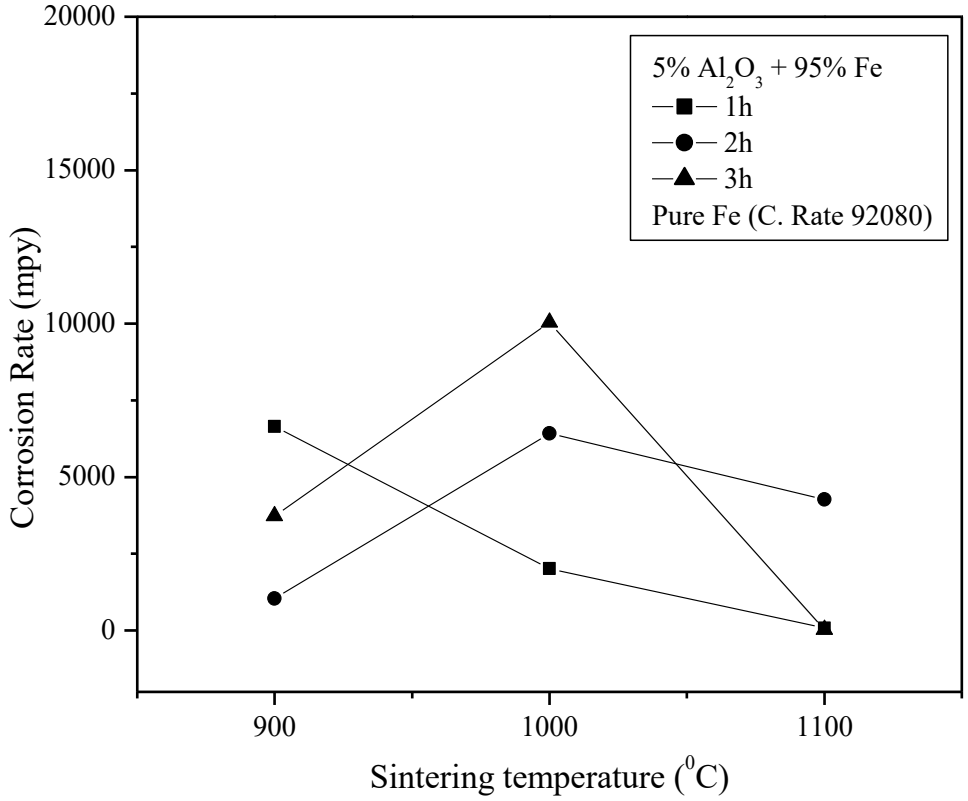

Fig. 9.3 Corrosion Rate vs. Sintering Temperature of Fe-5% Al_2O_3 nanocomposite specimens

It can be seen from the Tafel plots and the table that in the presence of alumina ceramic reinforcement, the Tafel curves are shifted to lower current regions, showing the protective tendency of the nanocomposites. From the table 9.1 and figs. 9.3 and 9.4 we observe that although the corrosion resistance of the nanocomposite specimen is very much higher than the pure iron specimen, there is no definite trend observed in variation of corrosion potential (E_{corr}) and corrosion current (I_{corr}) with change in sintering temperature and time. A similar observation has been made for dependence of hardness on sintering temperature and time. The explanation for such dependence as that for hardness can also be given to this observed behavior. The characteristics of the nanocomposite specimens depend on densification and formation of iron aluminate phase. The corrosion resistance is high for those specimens which have

higher density along with higher iron aluminate phase. It suggests that addition of alumina to iron matrix inhibits the corrosion of metal matrix nanocomposites [Tiwari et al. (2007)].

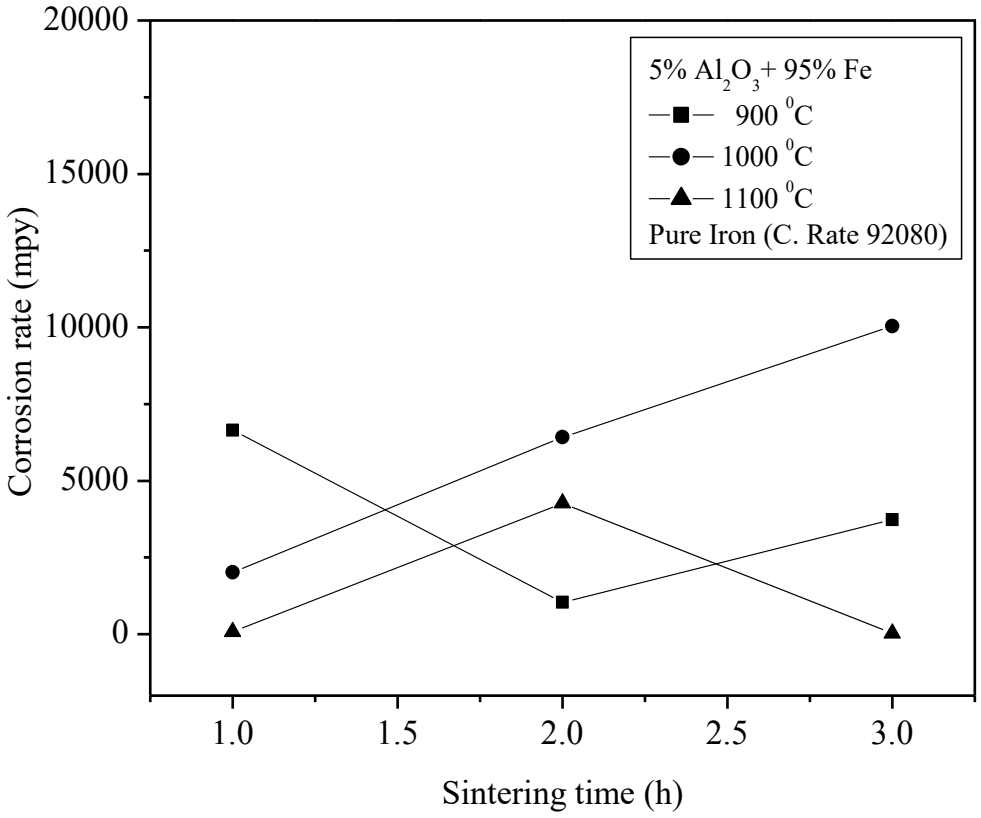

Fig. 9.4 Corrosion Rate vs. Sintering Time of Fe-5% Al_2O_3 nanocomposite specimens

9.1.2 Phase and Microstructure

In order to determine the cause for the lowest and highest amount of corrosion rate among differently sintered specimens and to find out the probable mechanism of corrosion inhibition, XRD and SEM investigations of different specimens have been carried out and the results of these investigations on 5AFe1000(3) and 5AFe1100(1) are presented here. The specimen 5AFe1100(1) showed the lowest corrosion whereas

the specimen 5AFe1000(3) showed the highest corrosion among the various synthesized MMNC specimens.

XRD patterns of the surfaces of these specimens after corrosion in 1N HCl are shown in Fig. 9.5. In the specimen 5AFe1100(1) a single peak of aluminum chlorate ($AlCl_3O_{12}$) is observed whereas the remaining two peaks are of iron (Fe) itself. Specimen 5AFe1000(3) shows two peaks of aluminum chlorate ($AlCl_3O_{12}$) and a single peak of iron. Thus, XRD patterns show the presence of iron (Fe) and aluminium chlorate ($AlCl_3O_{12}$) phases. Presence of aluminum chlorate peak can be attributed to the reaction taking place between iron and iron aluminate phase with hydrochloric acid.

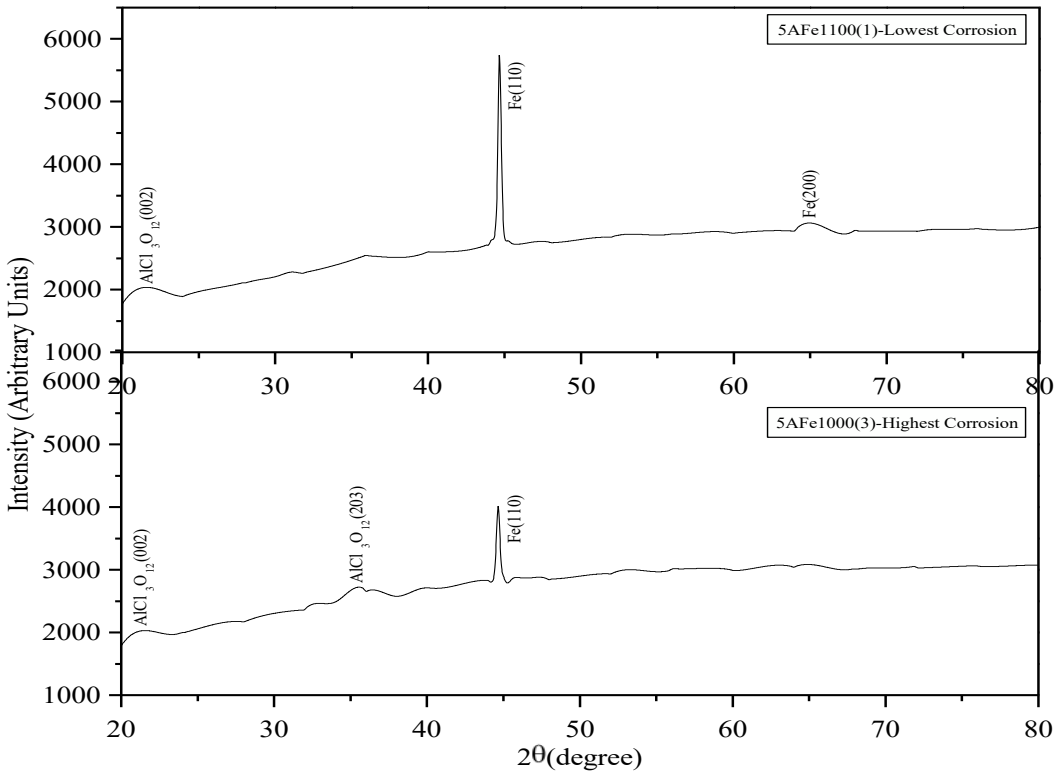

Fig. 9.5 XRD plots of Specimens (a) 5AFe1000(3) and (b) 5AFe1100(1)

It is quite evident that reaction product of the iron gets dissolved and goes towards the active sites therefore there is no peak due to the reaction between iron and

hydrochloric acid. Aluminium chlorate is sparingly soluble and it forms a layer on the surface of the specimen.

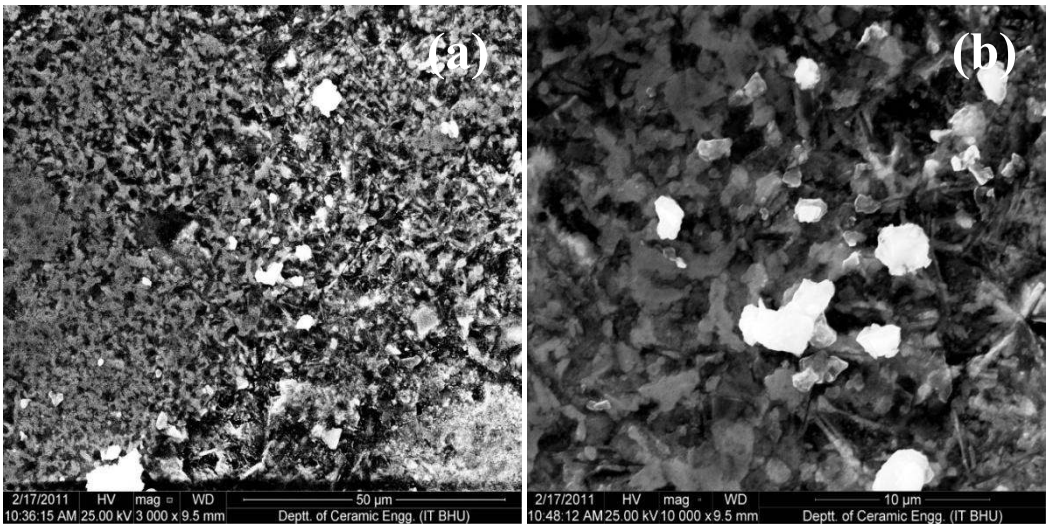

Fig. 9.6 SEM of specimen 5AFe1000(3) (a) 3000X and (b) 10000X magnification after corrosion in 1N HCl

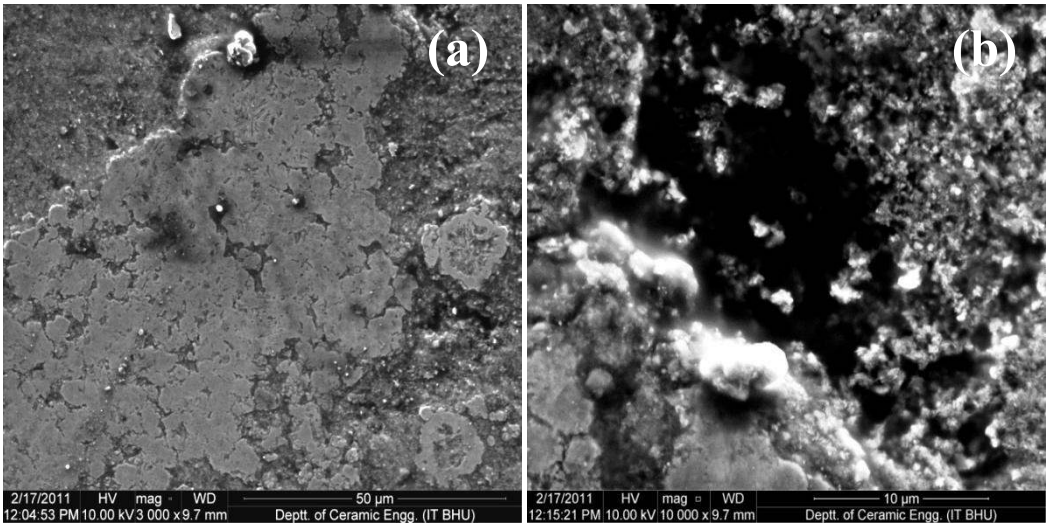

Fig. 9.7 SEM of specimen 5AFe1100(1) (a) 3000X and (b) 10000X magnification after corrosion in 1N HCl

Fig. 9.6 shows the scanning electron micrographs of specimen 5AFe1000(3) after immersion in the 1N HCl concentration. Fig. 9.6(a) shows the SEM micrograph taken at 3000X which shows the distribution of the particles due to the attack of HCl. Dissociation and pitting of the particles is very intense as a large amount of damage is

created by the acid attack. Fig. 9.6(b) shows the SEM micrograph of the same specimen at 10000X which shows the morphology or distribution of the grains. There are basically three type of the particles which are seen, pure white grains are of aluminum oxide, whitish grey are of aluminum chlorate and the rest black grains are of iron itself.

Similarly Fig. 9.7 shows the SEM micrographs of specimen 5AFe1100(1) which exhibits the minimum corrosion. Fig. 9.7(a) shows the distribution of the grains in a more uniform and distributed manner with least amount of shattering of the grains. This is due to the formation of the $FeAl_2O_4$ phase which has protected the specimen from the acid attack. Fig. 9.7(b) shows the micrograph of the same specimen at 10000X magnification. The dissociation of the particles is least, leading to lower amount of the formation of the aluminum chlorate phase.

The corrosion resistance of the specimen in the present case depends upon the sintering temperature and the sintering time. The specimens prepared in the present case undergo the reactive sintering process which improves the density, hardness, wear resistance and compressive strength of the specimens. During sintering beside densification there is a formation of nano size iron aluminate phase. At lower sintering temperature, the reactive sintering phenomena is slow, densification is less and thus the corrosion from the surface of the specimen is high (5AFe900(1)). For 1h of sintered specimens the densification value was highest for specimen sintered at 1100^oC for 1h (5AFe1100(1)) and thus the corrosion rate was lowest for this specimen. Thus, it is concluded that at lower sintering temperature and time of sintering the reaction between the aluminate phase and hydrochloric acid was higher and thus the corrosion rate increased significantly. It was also seen that the dissolution of the iron takes place completely thus leading towards the active site generation. As we move towards the specimen sintered for 2h the corrosion rate of the specimens varies as the variation of the aluminate phase formation. For the specimens sintered for 3h of time interval, the corrosion rate was found to be highest for specimen 5AFe1000(3). Overall it can be concluded that the iron aluminate phase

formation varies with the sintering temperature and time and this variation causes the change in the corrosion rate. The corrosion rate will increase in two cases first when the amount of iron aluminate phase formed is too low as in the case of 5AFe900(1) and second when there is an excessive increase in the aluminate phase formation i.e. in specimen 5AFe1100(3) and lower densification. However, the corrosion rate was found minimum for the specimen 5AFe1100(1).

9.2 Corrosion Behavior of 10% Al_2O_3 reinforcement

Iron - alumina based MMNC specimens having composition of 90 wt % Fe (electrolytic grade with 99.5% purity; 250-200 mesh (49-58 μm)) and 10 wt % Al_2O_3 (active; particle size of 70-230 mesh (63-210 μm)) were prepared using powder metallurgy technique. Green specimens prepared by compacting under a load of 7 tons were sintered in an argon atmosphere in the temperature range 900 - 1100°C for 1 - 3 hours. A nomenclature e.g. 10AFe1100(2) of different specimens is given indicating sintering temperature and time.

9.2.1 Tafel Polarization and Corrosion Behavior

The Tafel polarization curves of 10% Al_2O_3 reinforced specimens sintered for 3 different temperatures and time intervals are shown in Fig. 9.8, 9.9 and 9.10 respectively. Electrochemical parameters such as corrosion potential (E_{corr}), corrosion current density (I_{corr}), corrosion rate (C_r) and corrosion protection efficiency (μ_p) obtained from Tafel polarization curves are given in Table 9.2. Values of corrosion potential (E_{corr}), corrosion current density (I_{corr}), were evaluated from anodic and cathodic regions of Tafel plots. The linear segments of anodic and cathodic curves were extrapolated to corrosion potential to obtain corrosion current densities (I_{corr}). Anti-corrosive efficiency (μ_p %) was calculated from the measured I_{corr} values using the following relationship:

$$\mu_p\ \% = (I^o_{corr} - I^i_{corr}) / I^o_{corr} * 100$$

where I^o_{corr} and I^i_{corr} are values of corrosion current density for pure iron and for specimens with aluminium oxide as reinforcement respectively.

Figs 9.8 – 9.10 show tafel polarization plots of different specimens in Fe – 10% Al_2O_3 composite system. Fig. 9.11 shows the $E_{corr,}$ I_{corr} and corrosion rate vs. sintering temperature plots for different sintering times and Table 9.2 lists $E_{corr,}$ I_{corr}, corrosion rate and anti-corrosive efficiency of different specimens determined from these tafel plots. Fig. 9.8 shows the tafel polarization plots of specimens 10AFe900(2), 10AFe1000(2) and 10AFe1100(2) sintered for 2h at different sintering temperatures. It is seen from these graphs that the corrosion potential (E_{corr}) for the specimens 10AFe900(2), 10AFe1000(2) and 10AFe1100(2) was -577 mV, -540 mV and -531 mV respectively. It is also observed from Fig. 9.8 and table 9.2 that the corrosion rates of these three specimens are 803.2 mpy, 1542 mpy and 1955 mpy and the anti-corrosion efficiency (μ_p) is found to be 99.12%, 98.32% and 97.87% respectively. Therefore, it can be concluded from the above discussion that the lowest corrosion rate as well as the highest anti-corrosion efficiency was found for the specimen 10AFe900(2). It can be due to the reason that an optimum amount of nano iron aluminate phase has formed at this temperature and time of sintering.

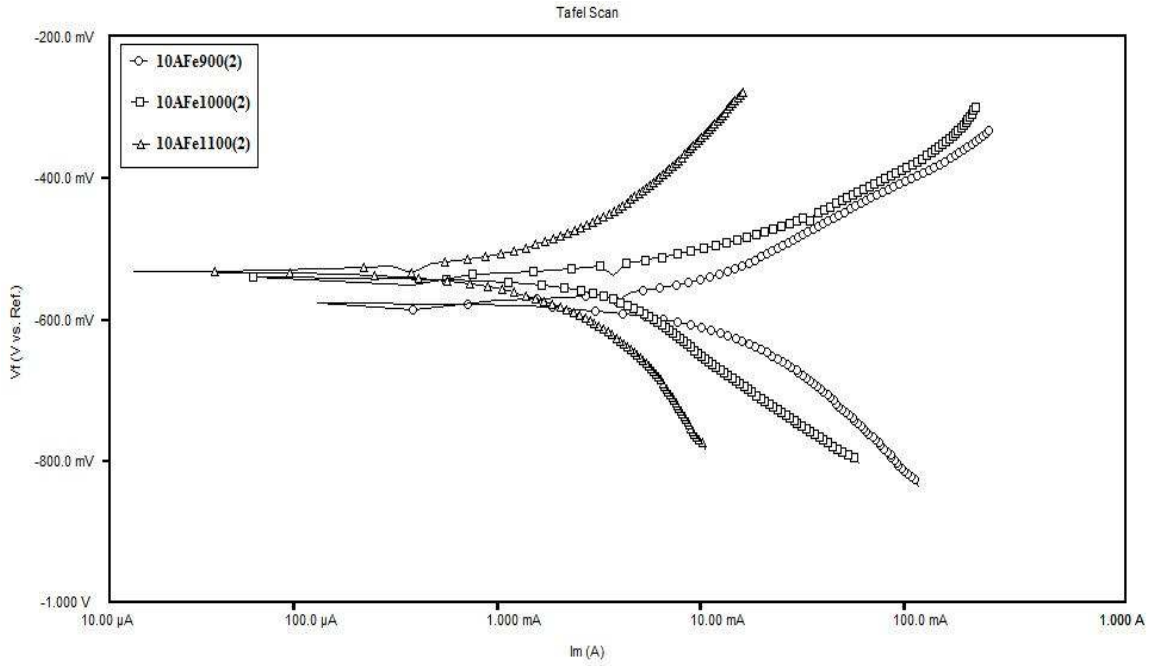

Fig. 9.8 Tafel polarization plots of specimens 10AFe900(2), 10AFe1000(2) and 10AFe1100(2) sintered for 2h at different sintering temperatures

This is formed by reaction between iron and alumina particles at sintering temperature of 900°C for 2 hours of sintering time which has lead towards the improvement in the corrosion resistance of the nanocomposite specimen.

Similarly, Fig. 9.9 shows the Tafel polarization plots of the specimens 10AFe1000(1), 10AFe1000(2) and 10AFe1000(3) sintered at 1000°C for different sintering times. For this set of specimens, the corrosion potential (E_{corr}) is found to be -611 mV, -540 mV and -595 mV [Fig. 9.9 and Table 9.3]. The corrosion rate for all the three specimens namely 10AFe1000(1), 10AFe1000(2) and 10AFe1000(3) are found to be 6049 mpy, 1542 mpy and 2491 mpy respectively. Further for these specimens the anti-corrosion efficiency (μ_p) is found to be 93.43%, 98.32% and 97.29% respectively. It can be explained on the basis of the above results that for the sintering temperature of 1000°C and sintering time of 2 hours, the corrosion characteristics were found to improve due to formation of the nano iron aluminate phase but at the same time the anti-corrosion efficiency for the specimen 10AFe1000(2) is reduced by 0.8024% in comparison to the specimen 10AFe900(2).

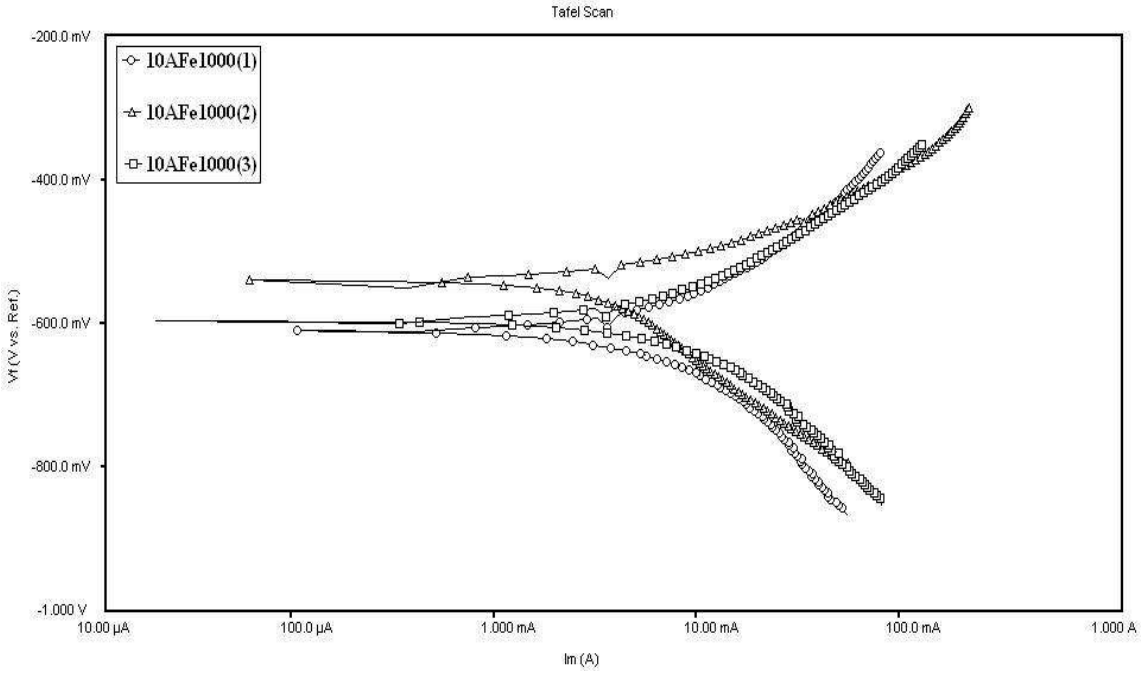

Fig. 9.9 Tafel polarization plots of specimens 10AFe1000(1), 10AFe1000(2) and 10AFe1000(3) sintered at 1000°C for different sintering times

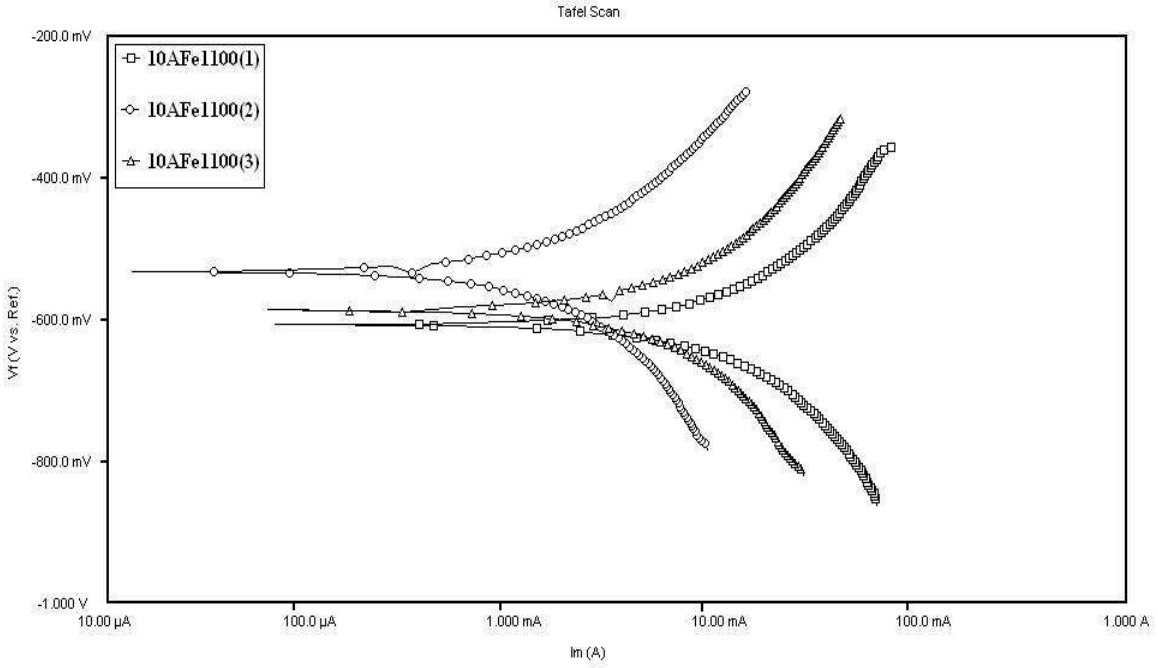

Fig. 9.10 Tafel polarization plots of specimens 10AFe1100(1), 10AFe1100(2) and 10AFe1100(3) sintered at 1100°C for different sintering times

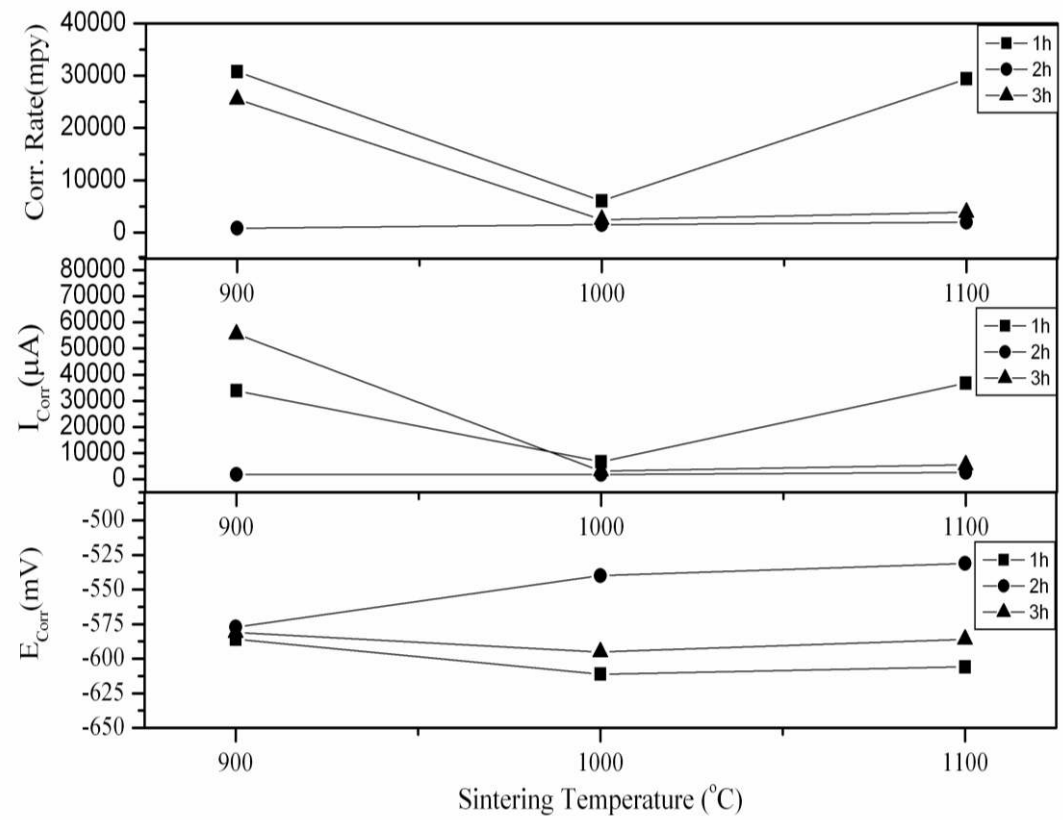

Fig. 9.11 E_{corr}, I_{corr} and Corrosion Rate vs. Sintering Temperature plots for different sintering time intervals

Fig. 9.10 illustrates the Tafel polarization plots of the specimens 10AFe1100(1), 10AFe1100(2) and 10AFe1100(3) sintered at 1100°C for different sintering times. From Fig. 9.10 and table 9.2, it is observed that these three specimens showed the corrosion potential (E_{corr}) values of -606 mV, -531 mV and -586 mV respectively. The corrosion rate and anti-corrosion efficiency (μ_p) of these three specimen namely 10AFe1100(1), 10AFe1100(2) and 10AFe1100(3) is found to be 29380 mpy, 1955 mpy and 3878 mpy and 68.09%, 97.87% and 95.78% respectively. From the above results it can be concluded that for 1100°C sintering temperature the best corrosion characteristics were found for the specimen 10AFe1100(2).

Table 9.2 E_{corr}, corrosion rate, I_{corr} and anti-corrosion efficiency (μ_p) values for the various 10% Al_2O_3 reinforced specimens

Sl. No.	Sample Code	E_{corr} (mV)	I_{corr} (µA)	Corrosion rate (C_r) (mpy)	μ_p (%)
1.	10AFe900(1)	-586	33900	30750	66.6051
2.	10AFe900(2)	-577	1750	803.2	99.1277
3.	10AFe900(3)	-581	55500	25480	72.3284
4.	10AFe1000(1)	-611	6640	6049	93.4307
5.	10AFe1000(2)	-540	1830	1542	98.3253
6.	10AFe1000(3)	-595	3130	2491	97.2947
7.	10AFe1100(1)	-606	36700	29380	68.0929
8.	10AFe1100(2)	-531	2510	1955	97.8768
9.	10AFe1100(3)	-586	5390	3878	95.7884
10.	Pure Iron	-559	200000	92080	-

Thus, on the basis of above results it can be concluded that among the nine specimens synthesized at different sintering temperature and time, the best anti-corrosion characteristics are found for the specimen 10AFe900(2). The reason for this can be that at lower sintering temperature of 900°C and sintering time of 2 hour, the reaction between iron and alumina particles is taking place due to which an optimum amount of nano size iron aluminate phase formation is taking place and this nano size phase is

inhibiting the corrosion of the nanocomposite specimens. It was also revealed that the dependence of corrosion parameters such as I_{corr} and corrosion rate on sintering temperature and time is similar to that of the hardness number. At 1000°C sintering temperature, the hardness number of the specimens sintered for 1h, 2h and 3h were found to be close to one another. I_{corr} and corrosion rate of the specimens sintered at 1000°C for different time of sintering showed almost the same values. Therefore, it can be concluded that at 1000°C whether we sinter the specimen for 1h, 2h or 3h the mechanical and electrochemical properties were found to improve almost identically due to an optimum formation of the iron aluminate phase.

It can also be seen from the Tafel plots (Fig. 9.8, 9.9 and 9.10) and table 9.2 that in the presence of aluminium oxide (Al_2O_3) reinforcement, the Tafel curves shifted towards the lower current regions, showing the anti-corrosion tendency of the nanocomposites. From the table 9.2 and Figs. 9.8, 9.9 and 9.10 we observe that there is no definite trend observed in the E_{corr} values for the nanocomposite specimens. It suggests that addition of alumina particles in iron matrix and thereby formation of iron aluminate phase inhibits the corrosion of metal matrix nanocomposites. It is noteworthy that the corrosion rate of the pure iron specimen was found to be 92080 mpy which is very much higher in comparison to the corrosion rate of the synthesized Fe-Al_2O_3 nanocomposite specimens. The best nanocomposite exhibited corrosion rate and anti-corrosion efficiency value as 803.2 mpy and 99.12% respectively. On the basis of above discussion it can be concluded that due to the existence of anodic and cathodic areas on iron surface it suffers corrosion. Pure Iron forms ferrous ions and two electrons at anode and at cathode it combines with proton and forms hydrogen gas. But when iron is mixed with aluminium oxide it leads to the formation of nano iron aluminate phase [Konopka and Ozieblo (2001)]. The formation of nano size iron aluminate causes following changes:

1) Decreases Wettability.

2) Increases Hydrophobicity.

3) Reduces Roughness of the surface.

All the above three factors significantly reduce corrosion of the formed nanocomposite specimens. In all the synthesized specimen of 5% Al_2O_3 reinforced specimens, the anti-corrosion efficiency was found to be above 90%. For 10% Al_2O_3 reinforced specimens, the anti-corrosion efficiency was found greater than 90% for all the specimens except for the specimen 10AFe900(1) and 10AFe900(3). A few specimens which are sintered at specific temperature for specific duration of time the protection efficiency is as high as 99% [10AFe900(2) and 10AFe1000(2)].

9.2.2 Phase and Microstructure

Fig. 9.12 shows the XRD plots of specimen 10AFe900(1) and 10AFe900(2) after corrosion in 1N HCl solution respectively. Specimen 10AFe900(1) shows the presence of aluminium chlorate ($AlCl_3O_{12}$), iron chloride ($FeCl_2$), iron (Fe) and aluminium oxide (Al_2O_3) phase. It was also found that in the present specimen the amount of the aluminium chlorate was much higher followed by some trace amounts of iron chloride phases. Similarly XRD pattern of the specimen 10AFe900(2) also shows the presence of aluminium chlorate ($AlCl_3O_{12}$), iron chloride ($FeCl_2$), iron (Fe) and aluminium oxide (Al_2O_3) phases. Overall, it was found that the intensity of the aluminium chlorate was more in the specimen 10AFe900(1) in comparison to the specimen 10AFe900(2). The amount of iron chloride phase was small in both the specimens. It is also seen that the corrosion rate of the specimen 10AFe900(1) is much more than that of the specimen 10AFe900(2) and thus due to this high corrosion rate, the formation of the aluminium chlorate phase is more in the specimen 10AFe900(1) in comparison to the specimen 10AFe900(2). The chemical reaction between 1N HCl solution and alumina particles has led to formation of the aluminum chlorate phase respectively.

Fig. 9.13 shows XRD plots of the specimen 10AFe1000(1) and 10AFe1100(2) after immersing specimen in 1N HCl solution.

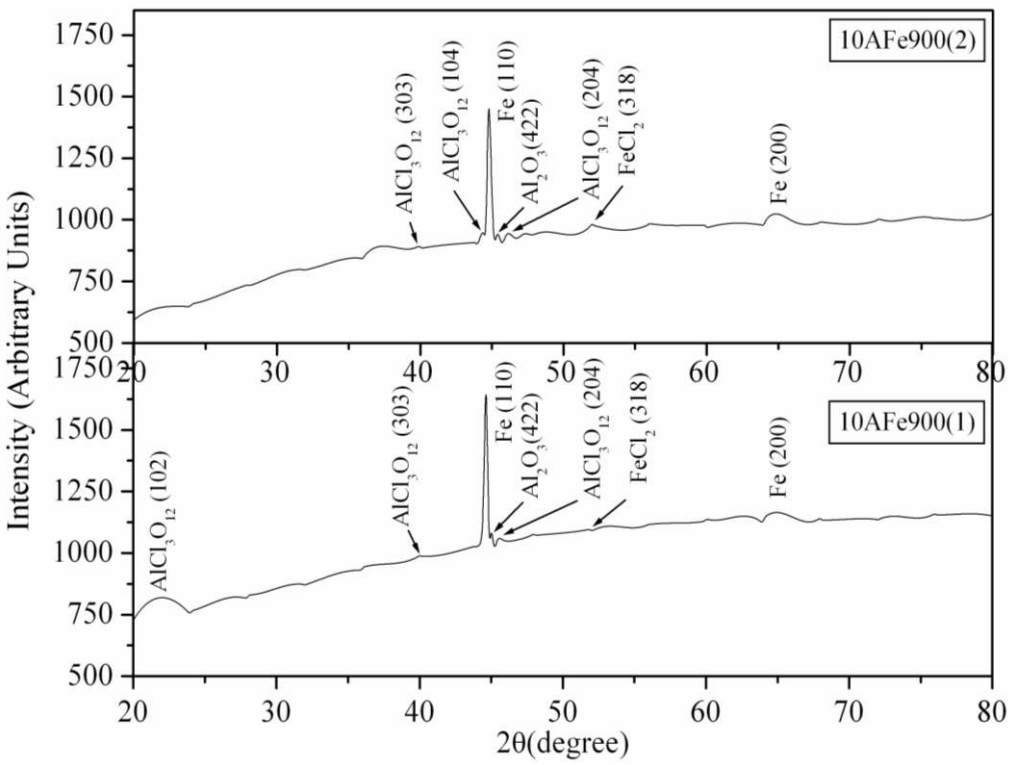

Fig. 9.12 XRD plots of specimen 10AFe900(1) and 10AFe900(2) after corrosion in 1N HCl solution

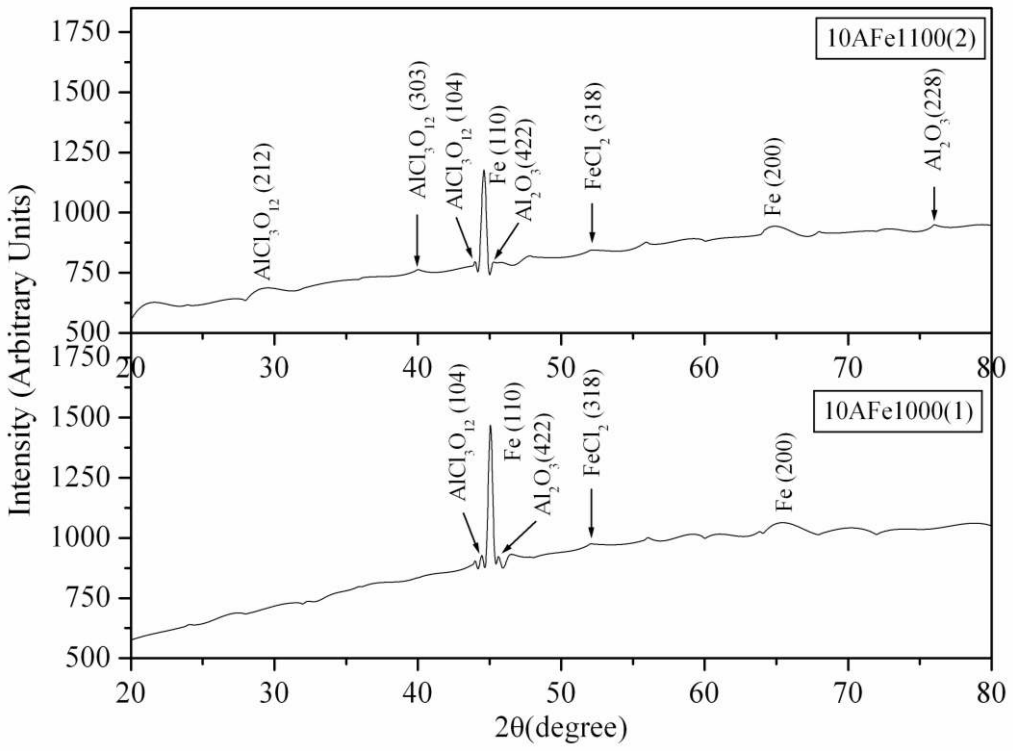

Fig. 9.13 XRD plots of specimen 10AFe1000(1) and 10AFe1100(2) after corrosion in 1N HCl solution

Both these specimens show the presence of the same phases which were present in the previous specimens i.e. aluminium chlorate ($AlCl_3O_{12}$), iron chloride ($FeCl_2$), iron (Fe) and aluminium oxide (Al_2O_3) respectively. It is seen from the plots that in the specimen, 10AFe1000(1) after corrosion, there is higher intensity lines of aluminium chlorate phase and weak XRD lines of iron chloride phase. Specimen 10AFe1100(2) also shows the presence of these two phases but the intensity of these phases is much lower than that of the specimen 10AFe1000(1). The specimen 10AFe1000(1) has higher corrosion rate in comparison to the specimen 10AFe1100(2). This seems that the amount of aluminium chlorate and iron chloride phases is more in specimen 10AFe1000(1) in comparison to the specimen 10AFe1100(2).

Scanning electron micrographs of the specimen were taken on the basis of (i) highest and lowest corrosion rate [Fig. 9.14 and 9.15] and (ii) highest and lowest corrosion potential [Fig. 9.16 and 9.17]. Fig. 9.14 shows the SEM images of the specimen 10AFe900(1) taken at (a) 500X (b) 2000X (c) 5000X and (d) 15000X magnifications after corrosion in 1N HCl solution respectively. Microstructure at 500X shows the presence of intense patches formed due to attack of HCl solution along with presence of some small size pores. The intensity of dark patches was so high that these could be very easily observed on the surface of the specimen. The micrograph of the same specimen at 2000X magnification is shown in Fig. 9.14(b) which shows the shattering of the conjugate particles along with the layering of the aluminium chlorate ($AlCl_3O_{12}$) particles. This aluminium chlorate particle forms after the reaction between chlorine and alumina particles respectively. Formation of the aluminium chlorate phase can be seen more clearly in the micrograph at 5000X [Fig. 9.14(c)]. It was observed that due to the attack of the HCl solution, elongation of the pores took place which can be seen very clearly in the micrograph shown in Fig. 9.14(d). The acid during the corrosion action has entered into the pores and it has generated the elongation. Since this specimen was sintered at lower temperature and for smaller time, the effect of acid attack was found to be more intense due to which the pore elongation and other distortions were generated on the specimen surface.

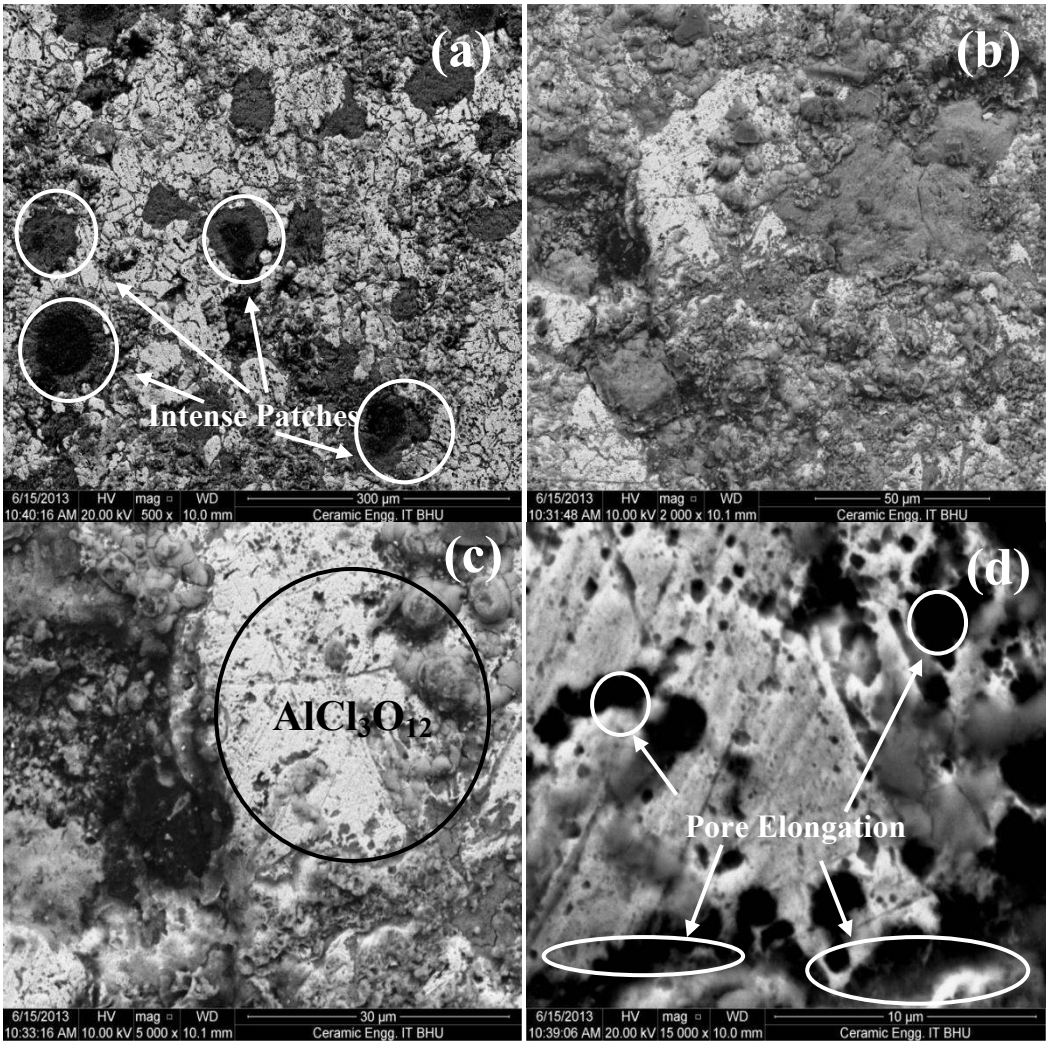

Fig. 9.14 SEM of specimen 10AFe900(1) at (a) 500X (b) 2000X (c) 5000X and (d) 15000 X magnifications after corrosion in 1N HCl

Fig. 9.15 shows the SEM of specimen 10AFe900(2) at (a) 500X (b) 2000X (c) 5000X and (d) 15000X magnifications after corrosion in 1N HCl solution. The micrograph at 500X shows the distortion of the particles with some light patches on the surface of the specimen. The less intensity of patches is due to attack of the acid on the specimen in comparison to the specimen 10AFe900(1). Fig. 9.15(b) which is the micrograph of the same specimen at 2000X magnification, reveals the formation of the aluminium chlorate particles on the surface of the specimen and it also shows some minor distortion among the particles of the nanocomposite system.

Fig. 9.15 SEM of specimen 10AFe900(2) at (a) 500X (b) 2000X (c) 5000X and (d) 15000X magnifications after corrosion in 1N HCl

Grain refinement and lowering of the grain size has also been observed in this micrograph. The grain refinement in the present case is caused due to entering of HCl in between the grains and grain boundaries. Micrograph of the same specimen at 5000X shown in Fig. 9.15(c) shows some bigger particles of iron aluminate phase and some aluminium chlorate particles distributed in between the various particles. The micrograph at 15000X magnification is shown in Fig. 9.15(d) which shows strong bonding between the constituent particles which remain in intimate contact even due to strong corrosion action. Therefore, it can be concluded that in the specimen 10AFe900(2), the complete reaction and an optimum amount of iron aluminate phase

formation has taken place due to which the corrosion resistance is improved manifold. Due to the improved corrosion resistance, the formation of the iron chloride phase cannot be distinguished clearly in the present micrograph.

Fig. 9.16 illustrates the SEM of specimen 10AFe1000(1) at (a) 500X (b) 2000X (c) 5000X and (d) 15000X magnifications after corrosion in 1N HCl solution. This specimen shows the highest corrosion potential value.

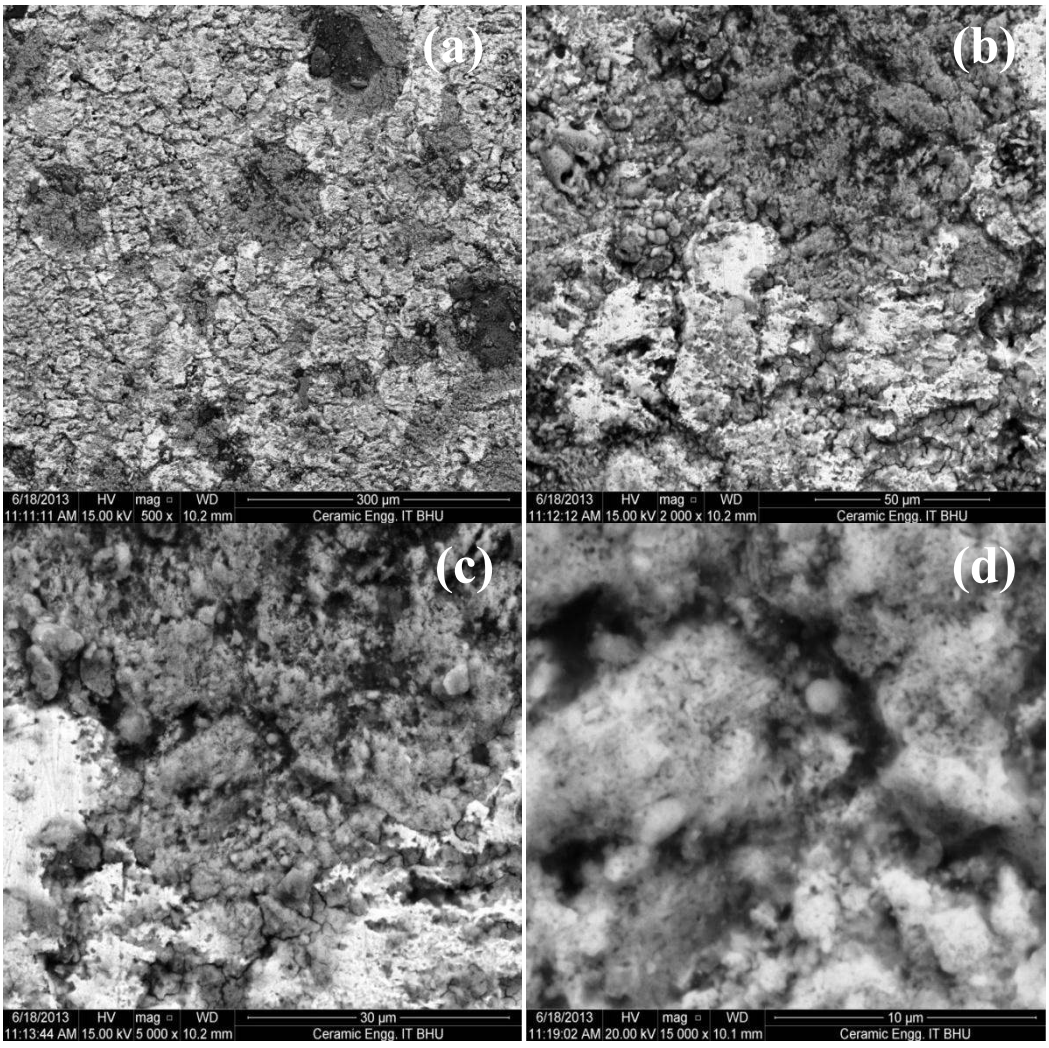

Fig. 9.16 SEM of specimen 10AFe1000(1) at (a) 500X (b) 2000X (c) 5000X and (d) 15000X magnifications after corrosion in 1N HCl

Micrograph of the specimen at 500X [Fig. 9.16(a)] shows the formation of some patches as well as the distributed type grains of the constituent particles. It also illustrates some micro cracks formed at the intergranular sites of the constituent particles. Fig. 9.16(b) shows the microstructure of the same specimen at 2000X magnification which shows an agglomeration amongst some particles of aluminium chlorate. It also shows some particles being separated due to the corrosion action. This agglomeration can be due to very small size of the aluminium chlorate particles after the electrochemical activity is completed on the nanocomposite specimen. Some particles which are not agglomerated are dispersed due to loosening of the bonds during the corrosion action. Formation of the aluminium chlorate phase can be seen much more clearly in the Fig 9.16(c) which is the microstructure of the same specimen at 5000X magnification. It can also be seen in the same micrograph that the reduction in the grain size has also taken place. The reduction in the grain size and formation of finer grains of the iron aluminate phase can also be seen much more clearly in the micrograph at 15000X magnification [Fig. 9.16(d)].

Fig. 9.17 shows the SEM of specimen 10AFe1100(2) at (a) 500X (b) 2000X (c) 5000X and (d) 15000X magnifications after corrosion in 1N HCl solution. The present specimen shows the lowest corrosion potential. The SEM of the specimen at 500X magnification [Fig. 9.17(a)] shows the presence of the constituent particles along with the presence of some small cavities on the surface of the specimen. The outer periphery of the cavities is dark in nature. The cavities present on the specimen surface and the corresponding darkness present on the periphery are formed during the corrosion action. The same micrograph when viewed at 2000X magnification as illustrated in Fig. 9.17(b) shows the peeling of the material from the top surface of the specimen along with that it also shows the formation of some nano size aluminium chlorate phase deposited on the surface. Fig. 9.17(c) shows the SEM of the same specimen at 5000X magnification which shows the formation of a small number of particles of the constituent phase due to the corrosion action. It also shows some wide patch of aluminium chlorate phase.

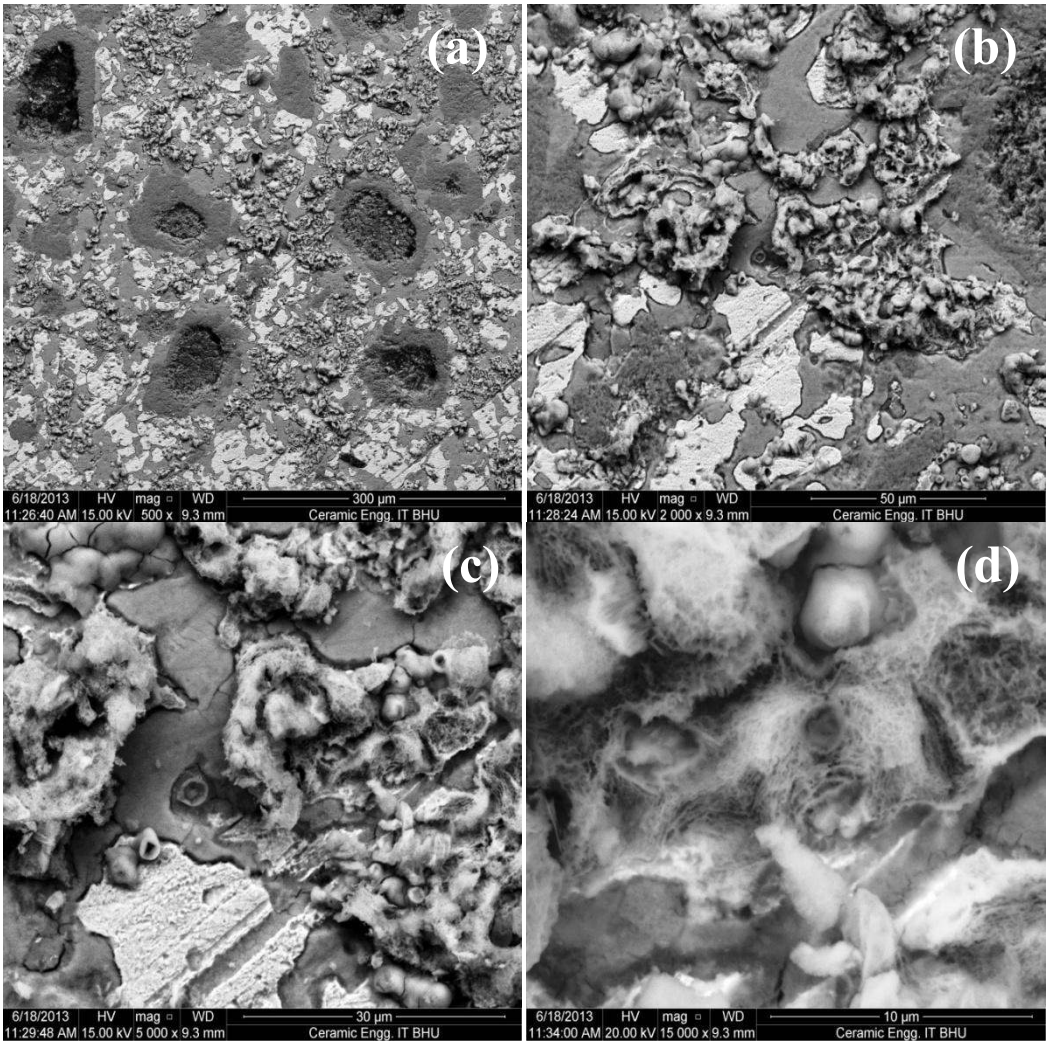

Fig. 9.17 SEM of specimen 10AFe1100(2) at (a) 500X (b) 2000X (c) 5000X and (d) 15000X magnifications after corrosion in 1N HCl

The dispersed particles in the form of nano rods can be seen more clearly in the micrograph at 15000X magnification illustrated in Fig. 9.17(d). This micrograph also shows some iron chloride phase which is present in the dissolved form.

9.3 Corrosion Behavior of CoO Doped Fe-Al_2O_3 Metal Matrix Nanocomposites

To study the effect of CoO doping on the corrosion behavior of Fe-Al_2O_3 metal matix composites, a few CoO doped specimens were prepared. Powders of electrolytic grade iron metal (99.5% purity and particle size 250-300 mesh (49-58 µm)) and

active aluminum oxide (particle size 70-230 mesh (63-210μm)) and cobalt oxide (99% purity) were used as starting materials. Composition of the composite was 90% Fe and 10% Al_2O_3 by weight. 0.5 and 1.0% by weight of the cobalt oxide was added as a dopant in this composite system. Appropriate mixtures of Fe, Al_2O_3, CoO and binder were dry ball milled for 2 hours using zirconia balls as the grinding and mixing media with powder to ball ratio of 1:2. Cylindrical compacts were sintered in an argon atmosphere at 1100°C for 1h. A nomenclature e.g. 10AFe0.5Co1100(1) is given to each specimen. Here A denotes the aluminum oxide, Fe denotes iron, 0.5Co denotes the percentage of cobalt oxide, 1100 denotes the sintering temperature and 1 denotes time of sintering in hr. The specimens for the corrosion measurement were cut with 12 mm diameter and 2 mm height. After measurement the specimen were washed thoroughly and was kept in hot air oven to remove the volatile matter present in it. These specimens were used for the XRD, SEM along with EDAX studies.

9.3.1 Tafel Polarization and Corrosion Behavior

The Tafel polarization curves for pure iron specimen and three different specimens containing fixed amount of aluminium oxide (Al_2O_3) and varying amount of cobalt oxide (CoO) in 1N HCl solution are shown in Fig. 9.18 (Pure Fe, Pure Fe+0.5% CoO 10AFe0.5Co1100(1) and 10AFe1.0Co1100(1)). The linear segments of anodic and cathodic curves were extrapolated to corrosion potential to obtain corrosion current densities (I_{corr}). Electrochemical parameters such as corrosion potential (E_{corr}), corrosion current density (I_{corr}), corrosion rate (C_r) and anti-corrosive efficiency (μ_p) obtained from Tafel polarization curves are given in Table 9.3. Values of corrosion potential (E_{corr}), corrosion current density (I_{corr}), were evaluated from anodic and cathodic regions of Tafel plots. Anti-corrosive efficiency was evaluated from the measured I_{corr} values using the relationship:

$$\mu_p\ \% = (I^o_{corr} - I^i_{corr}) / I^o_{corr} * 100$$

where I^o_{corr} and I^i_{corr} are values of corrosion current density for pure iron and for specimens with aluminium oxide and cobalt oxide as reinforcement respectively.

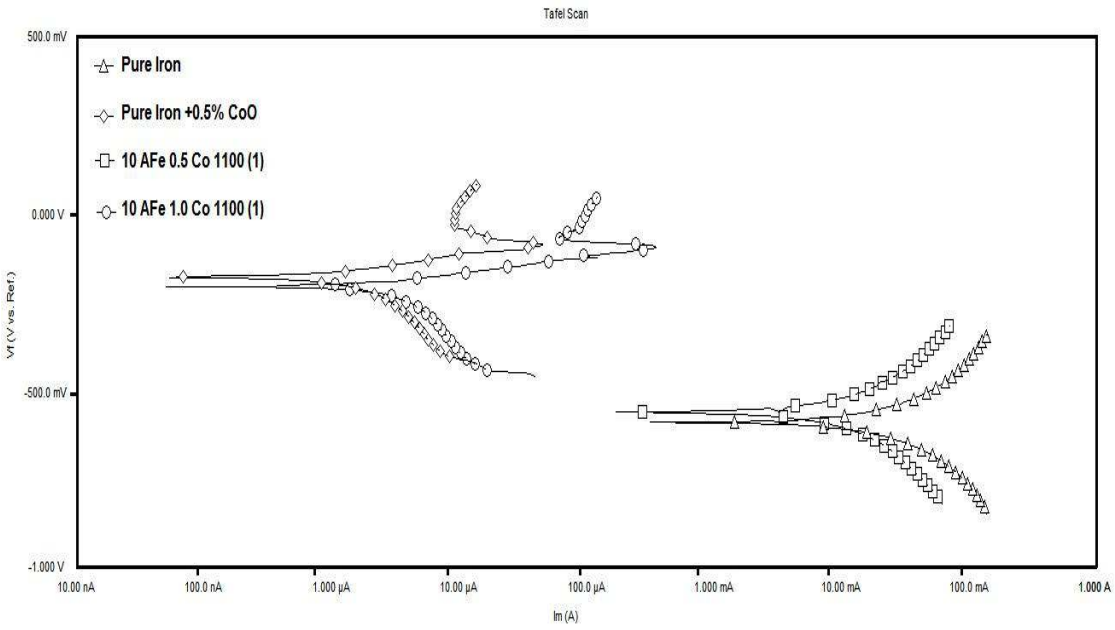

Fig. 9.18 Tafel Polarization plots of cobalt oxide doped specimens

It is observed from the results (Fig. 9.18 and Table 9.3) that the corrosion rate for the pure iron specimen [66540 mpy] and 10AFe0.5Co1100(1) [19810 mpy] is high in comparison to the corrosion rate for the specimens 10AFe1.0Co1100(1) [1.844 mpy] and Pure Fe+0.5% CoO [0.731 mpy]. Corrosion potential for the specimen pure iron and 10AFe0.5Co1100(1) is found to be -582 and -554 mV whereas those that of the specimen 10AFe1.0Co1100(1) and Pure Fe+0.5% CoO are found out to be -201 mV and -175 mV respectively. Therefore, corrosion potential (E_{corr}) for the synthesized specimens varies from -582 to -175 mV. Specimen Pure Fe+0.5% CoO showed maximum shift of E_{corr} (407 mV) toward noble direction followed by 10AFe1.0Co1100(1). Corrosion current for the specimens pure iron and 10AFe0.5Co1100(1) is found out to be 145000 µA and 43200 µA whereas that of the specimen 10AFe1.0Co1100(1) and pure Fe+0.5% CoO is found to be 4.02 µA and 1.59 µA respectively. It is seen that by the addition of 10% Al_2O_3 and 0.5% CoO to the specimen 10AFe0.5Co1100(1), the anti-corrosion efficiency improved by 70.2284%. For specimen 10AFe1.0Co1100(1), the addition of 10% Al_2O_3 and 1.0% CoO in iron matrix gives 99.9972% anti-corrosion efficiency.

Table 9.3 E_{corr}, corrosion rate, I_{corr} and anti-corrosion efficiency (μ_p) values for the CoO doped specimens

Sl. No.	Sample Code	E_{corr} (mV)	I_{corr} (µA)	Corrosion rate (mpy)	μ_p (%)
1.	Pure Fe	-582	145000	66540	-
2.	Pure Fe+0.5% CoO	-175	1.59	0.731	99.9989
3.	10AFe0.5Co1100(1)	-554	43200	19810	70.2284
4.	10AFe1.0Co1100(1)	-201	4.02	1.844	99.9972

It is interesting to note that corrosion rate for the specimen pure Fe+0.5% CoO is minimal i.e. 0.731 mpy. This means that by addition of 0.5% CoO to pure iron specimen anti-corrosion efficiency becomes 99.9989%. Superior corrosion resistance of the specimens 10AFe1.0Co1100(1) and Pure Fe+0.5% CoO can be attributed to the existence of nano size particles of Al_2O_3 and CoO which instantly undergoes passivation forming film on the iron surface which protects the corrosion of iron in HCl solution. Similar results for the formation of passivation film due to the presence of chromium in the stainless steel reported by Song (2005). Gupta and Birbilis (2015) also reported the presence of a passivation film while studying the corrosion behavior of chromium containing nano crystalline stainless steel. Our results of CoO doped Fe-Al_2O_3 metal matrix nancomposites are in accordance with the results of Song (2005) as well as Gupta and Birbilis (2015). It was also seen from these results that the corrosion behavior of the specimen has generated finer nano size particles and nano size rods structure on the surface of the specimen thereby inhibiting corrosion and improving the overall corrosion resistance of the specimens. The presence of nano size particles and rods has been corroborated by SEM and corresponding EDAX analysis.

9.3.2 Phase and Microstructure

Fig. 9.19 shows XRD patterns of corroded surfaces of the specimens (a) Pure Fe (b) 10AFe0.5Co1100(1) (c) 10AFe1.0Co1100(1) and (d) Pure Fe+0.5% CoO specimens respectively. Pure Fe specimen shows the presence of pure iron phase. Specimen

10AFe0.5Co1100(1) shows the presence of a smaller peak of iron and presence of some peak of cobalt chlorate ($CoCl_2$).

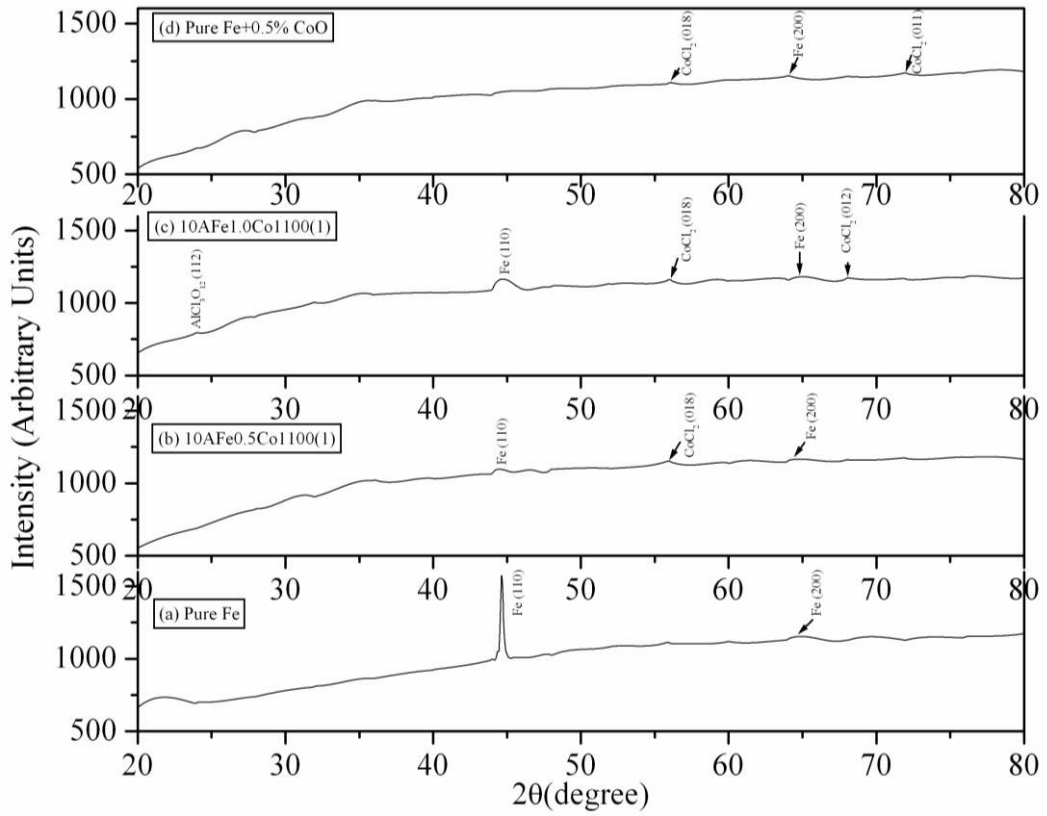

Fig. 9.19 XRD patterns of the corroded surfaces of (a) Pure Fe (b) 10AFe0.5Co1100(1) (c) 10AFe1.0Co1100(1) and (d) Pure Fe+0.5% CoO specimens respectively

Similarly the specimen 10AFe1.0Co1100(1) showed presence of aluminum chlorate ($AlCl_3O_{12}$) and cobalt chlorate ($CoCl_2$) phases respectively. Finally the specimen having pure Fe with 0.5% CoO showed presence of some smaller peaks of iron and of cobalt chlorate phases respectively. From the XRD results, it can be seen that there is more amount of cobalt chlorate phase and at the same time there is a presence of aluminum chlorate phase which is formed on the specimen surface as a result of the corrosion action.

Fig. 9.20 shows the SEM micrograph of Pure Iron specimen after corrosion in 1N HCl at (a) 1000X (b) 2000X and (c) 5000X magnification respectively. The micrograph at 1000X (Fig. 9.20(a)) shows the heavily distributed grains of iron after

attack of hydrochloric acid on the specimen surface. The same specimen when viewed at 2000X (Fig. 9.20(b)) magnification shows the presence of some micron sized particles whose size lies in the range of 5-10µm. The micrograph of the same specimen at 5000X magnification [Fig. 9.20(c)] shows the distributed pore structure on iron grains and some grains having different morphology than the iron grains.

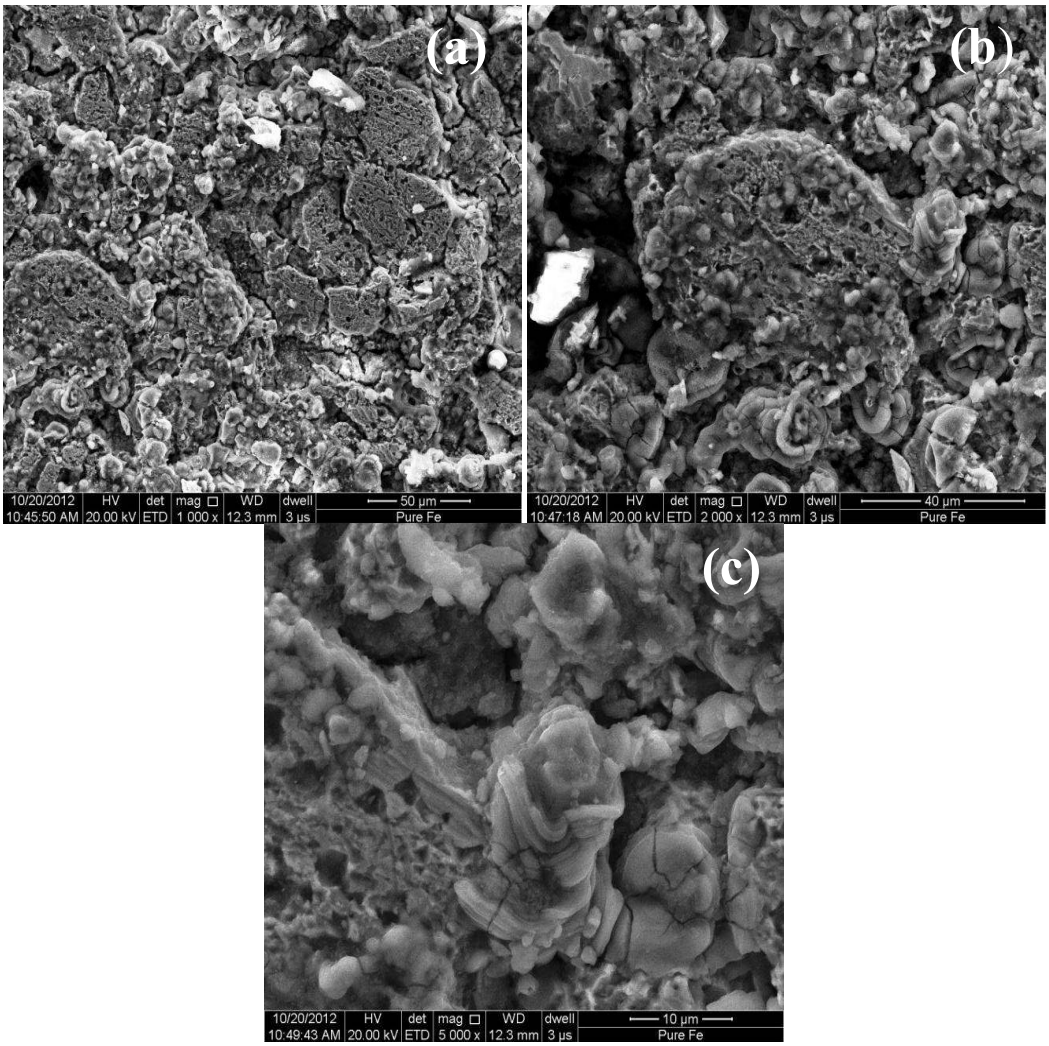

Fig. 9.20 SEM micrograph of Pure Iron specimen after corrosion in 1N HCl at (a) 1000X (b) 2000X and (c) 5000X magnification respectively

XRD studies reveal the presence of different phases in the specimen in totality and if the concentration of some phase is small it is not being detected by the instrument. In order to confirm the results of XRD studies and to microstructurally identify the phases EDAX characterization was carried out. Therefore, we have characterized

corroded surfaces of the specimen with EDAX. Different regions and morphology of the specimens were scanned for the compositional analysis. Fig. 9.21 shows the SEM image of Fig. 9.20(c) and EDAX patterns of different regions (a, b, and c) of microstructure. Pattern "a" corresponds to the pitting surface of the specimen, whereas patterns "b" and "c" correspond to different particles present on the surface.

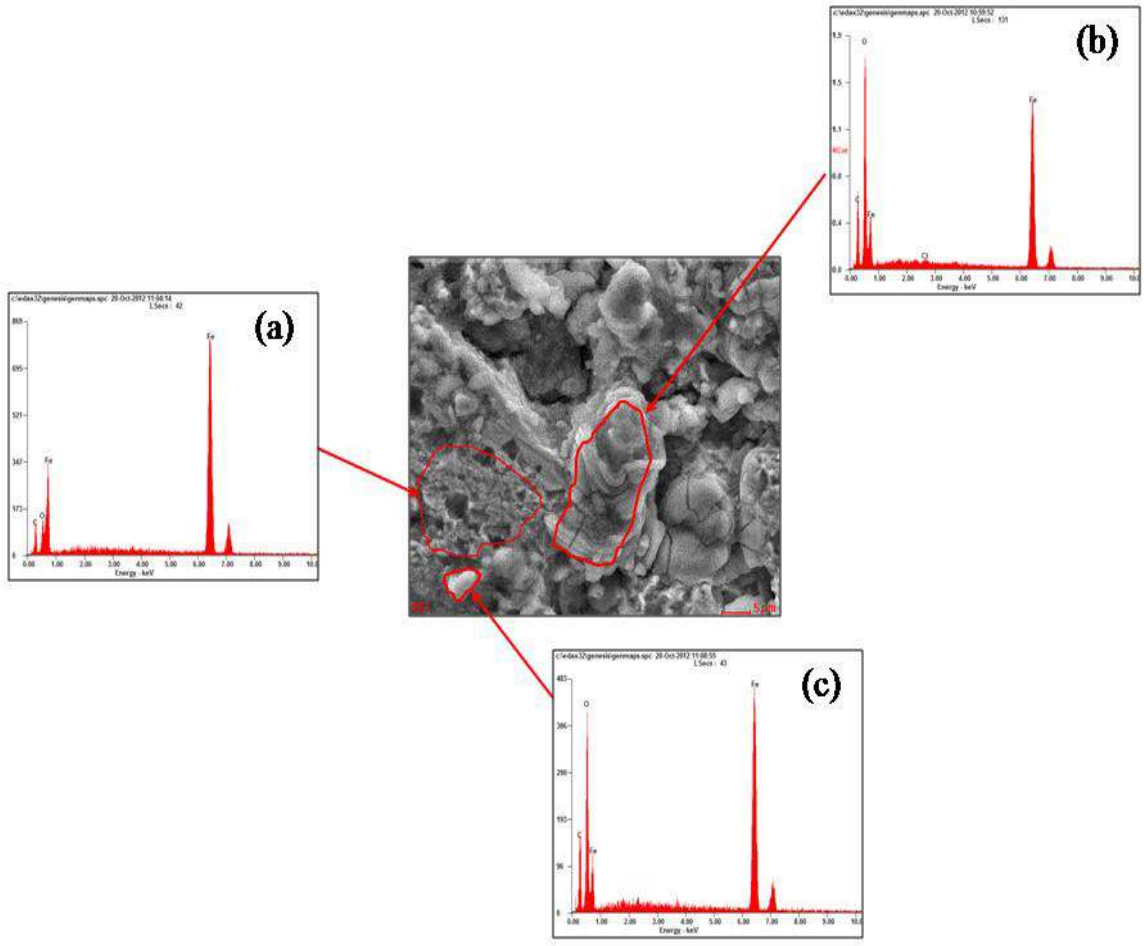

Fig. 9.21 SEM and EDAX of different regions (a, b, and c) for pure iron specimen after corrosion in 1N HCl at 10000X magnification

The elemental profile determined from these EDAX for different regions of microstructure are given in Table 9.4. The overall energy dispersive spectroscopic analysis (EDAX) shows the presence of three elements namely carbon (C), oxygen (O) and iron (Fe) respectively. In the region "a" carbon is 18.33 wt%, oxygen is 05.21 wt% and iron is 76.46 wt%. Region "b" shows 26.59 wt% of carbon, 27.10 wt% oxygen and 46.00 wt% iron.

Table 9.4 Elemental profile of various constituents of pure iron specimen after corrosion

Composition	a		b		c	
	Wt%	At%	Wt%	At%	Wt%	At%
C	18.33	47.37	26.59	46.70	26.39	48.97
O	05.21	10.11	27.10	35.74	21.79	30.36
Cl	--	--	00.31	00.18	--	--
Fe	76.46	42.51	46.00	17.37	51.81	20.67

Apart from this it also shows some traces of Chlorine 00.31% respectively. Similarly region "c" shows 26.39 wt% of carbon, 21.79 wt% of oxygen and 51.81 wt% of iron. The presence of carbon indicates that some residue of binder (dextrin) burn out remains in the specimen in the form of carbon. It implies that complete burn out of dextrin is not taking place at sintering temperature under inert atmosphere. It was indicated to us that the observation of excess carbon may be due to some instrumental conditions and/or usage of carbon tape for mounting the specimen. Atomic fraction of iron in region "a" is higher in comparison to its atomic fraction in particles "b" and "c". Atomic fraction of oxygen is lower in region "a" in comparison to its fraction in particles "b" and "c". Increased fractions of oxygen in particles "a" and "b" indicate that these are oxidative residue of corroded iron.

Fig. 9.22 shows the SEM of the specimen 10AFe0.5Co1100(1) after corrosion in 1N HCl solution at (a) 1000X (b) 2000X and (c) 5000X magnification respectively. Microstructure of the specimen at 1000X (Fig. 9.22(a)) shows the presence of shattered grains of iron, alumina and cobalt oxide particles respectively. The shattering of the particles in the present micrograph is less than that of pure Fe specimen which in itself shows the protective nature from the alumina and cobalt oxide nano particles against the attack of HCl solution. Fig. 9.22(b) shows the micrograph at 2000X which reveals the dispersion of the various particles and it also shows the bursting of the particles due to attack of HCl solution itself. The bursting of the particles and an inner view of the grains can be observed in Fig. 9.22(c) which is the micrograph of the same specimen at 5000X magnification. It can also be seen that the anti-corrosion efficiency of the present specimen (10AFe0.5Co1100(1)) is found

to be better in comparison to pure iron specimen and was found to be comparable to specimen 10AFe1.0Co1100(1).

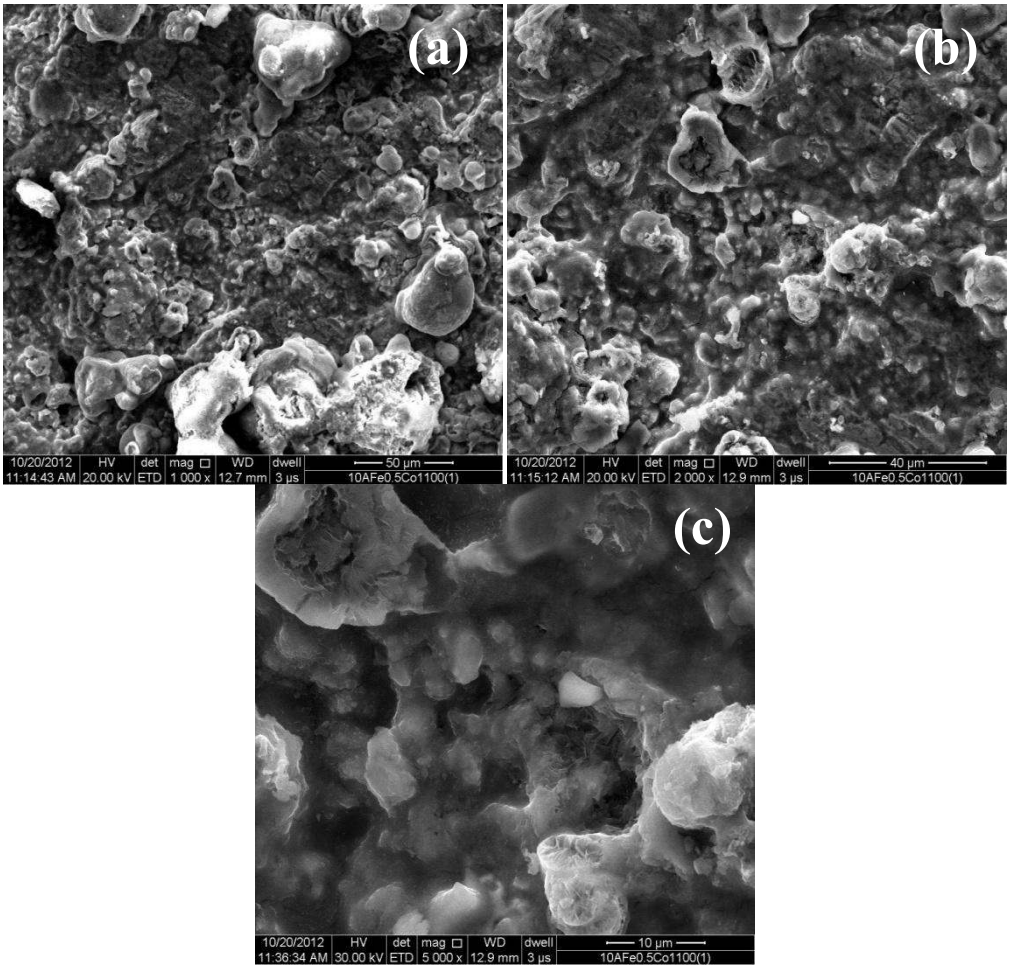

Fig. 9.22 SEM of the specimen 10AFe0.5Co1100(1) after corrosion in 1N HCl at (a) 1000X (b) 2000X and (c) 5000X magnification respectively

Fig. 9.23 shows SEM image of the Fig. 9.22(b) and EDAX patterns of different regions (a, b, c and d) of the microstructure. The corresponding elemental profile of the different regions shown in the micrograph is also given in Table 9.5. The overall EDAX analysis recorded at different region shows the presence of basically four elements namely carbon (C), oxygen (O), aluminium (Al) and iron (Fe) respectively. EDAX is done on 4 different particles i.e. (Region a, b, c and d). Region "a" shows 13.69 wt% carbon, 11.17 wt% oxygen, 01.93 wt% aluminium and 73.21 wt% iron. Region "b" shows 21.43 wt% carbon, 19.68 wt% oxygen, 01.51 wt% aluminium and 57.38 wt% iron. Region "c" shows 20.84 wt% carbon, 33.97 wt% oxygen, 02.98 wt%

aluminium and 42.21 wt% iron. The region d shows 18.53 wt% carbon, 21.41 wt% oxygen, 07.52 wt% aluminium and 52.54 wt% iron.

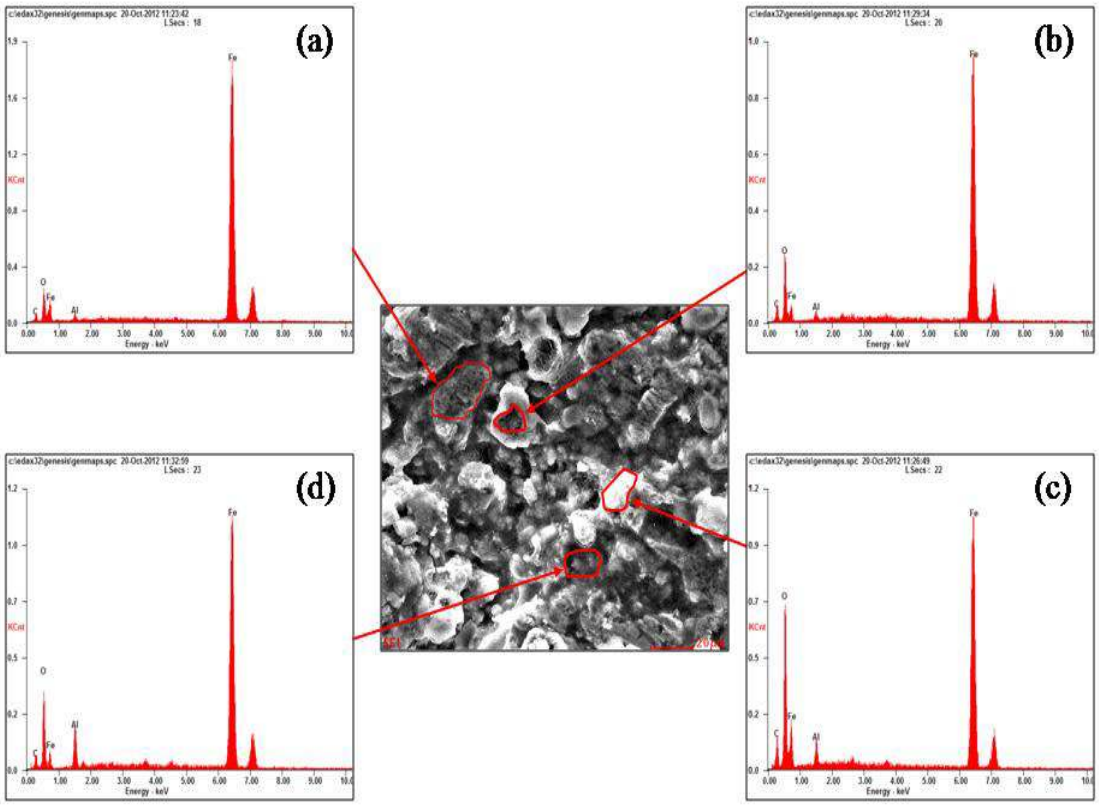

Fig. 9.23 SEM and EDAX of different regions (a, b, c and d) of the specimen 10AFe0.5Co1100(1) after corrosion in 1N HCl at 2000X magnification

Table 9.5 Elemental Profile of various constituents of 10AFe0.5Co1100(1) specimen after corrosion

Composition	a		b		c		d	
	Wt%	At%	Wt%	At%	Wt%	At%	Wt%	At%
C	13.69	35.39	21.43	43.54	20.84	36.72	18.53	37.62
O	11.17	21.69	19.68	30.02	33.97	44.95	21.41	32.63
Al	01.93	02.22	01.51	01.36	02.98	02.34	07.52	06.80
Fe	73.21	40.70	57.38	25.07	42.21	16.00	52.54	22.94

From the above discussion it can be concluded that there is presence of iron as the major phase, followed by carbon and aluminium. Iron and alumina were present in the starting material so it is verified from there itself. Presence of carbon is due to the removal of the binder from the specimen, which has sticked to the specimen surface

itself. It is also observed that cobalt oxide is present in the specimen but its presence is not detected in the EDAX analysis. This may be due to the fact that because amount of cobalt oxide is only 0.5 wt% therefore it cannot be detected by the instrument. Atomic fraction of iron is high in the region “a” in comparison to region “b” and “c”. However atomic fraction of aluminium is higher in the region “d” in comparison to region “a”, “b” and “c”. In region “d” aluminium is present and the perspective compound is aluminum chlorate. Atomic fraction of oxygen was found to be highest in the region “c”. From this elemental profile of different regions as given in table 9.5; region “a” shows the corroded iron grain, “b” shows the inside structure of bursted grain, “c” and “d” shows the alumina grains.

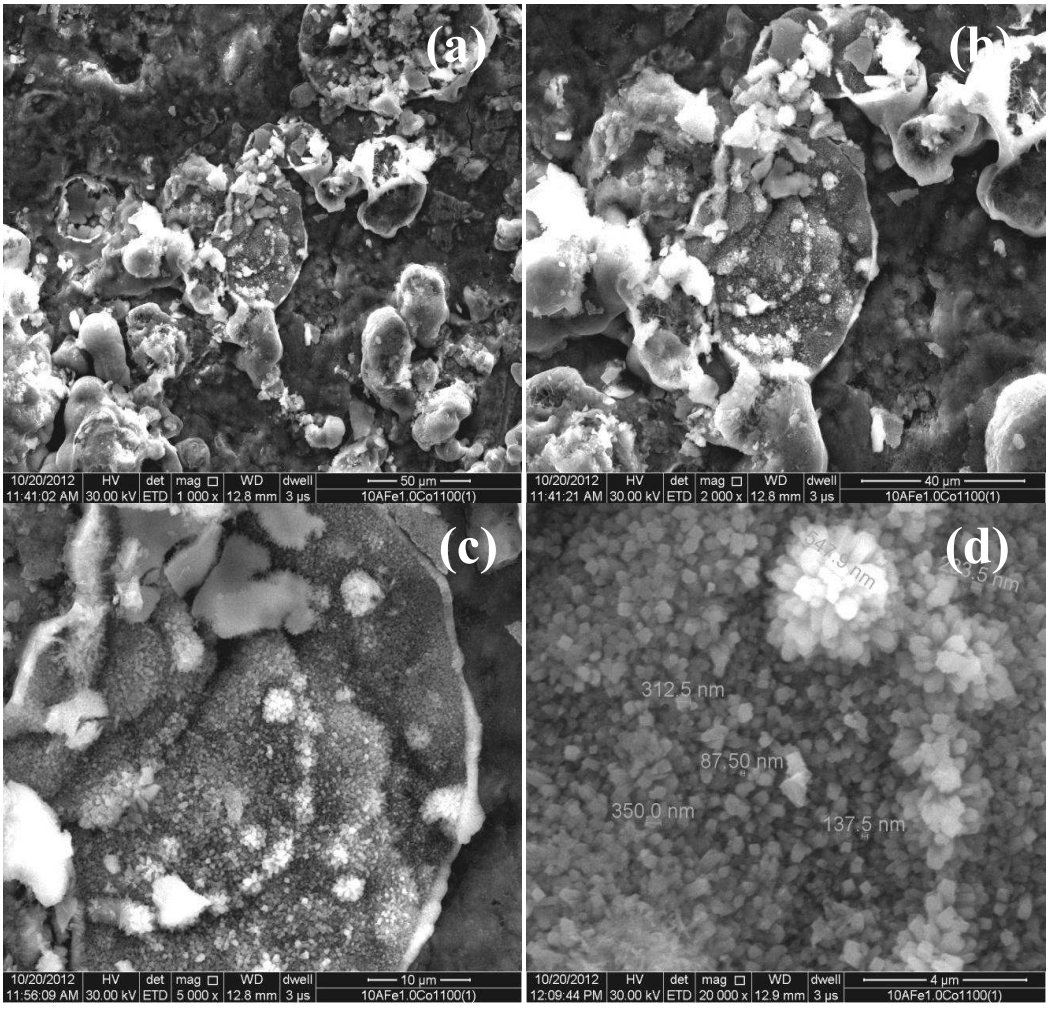

Fig. 9.24 SEM of the specimen 10AFe1.0Co1100(1) after corrosion in 1N HCl at (a) 1000X (b) 2000X (c) 5000X and (d) 20000X magnification respectively

Fig. 9.24 shows the SEM of the specimen 10AFe1.0Co1100(1) after corrosion in 1N HCl at (a) 1000X (b) 2000X (c) 5000X and (d) 20000X magnification respectively. The present specimen shows the highest anti-corrosion efficiency and its corrosion resistance was found to be far better in comparison to pure iron specimen. Fig. 9.24(a) shows the SEM of the specimen at 1000X which shows the conjugated grains of the constituent phases. It was seen from this micrograph that there was no disturbance in the morphology of the grains in the present specimen as compared to the pure iron and 10AFe0.5Co1100(1) specimen. The micrograph of the same specimen when viewed at 2000X magnification (Fig. 9.24(b)) revealed 2-4 µm size particles of constituent phases. Fig. 9.24(c) shows the interior view of the same specimen at 5000X magnification. The microstructure shows 1-2 µm size particles of aluminium chlorate ($AlCl_3O_{12}$) and cobalt chlorate ($CoCl_2$) phases. SEM micrograph of the same specimen at 20000X magnification is shown in Fig. 9.24(d) which shows nanosize particles of $AlCl_3O_{12}$ and $CoCl_2$ phases. The size of nano particle lies in the range of 88 – 548 nm respectively.

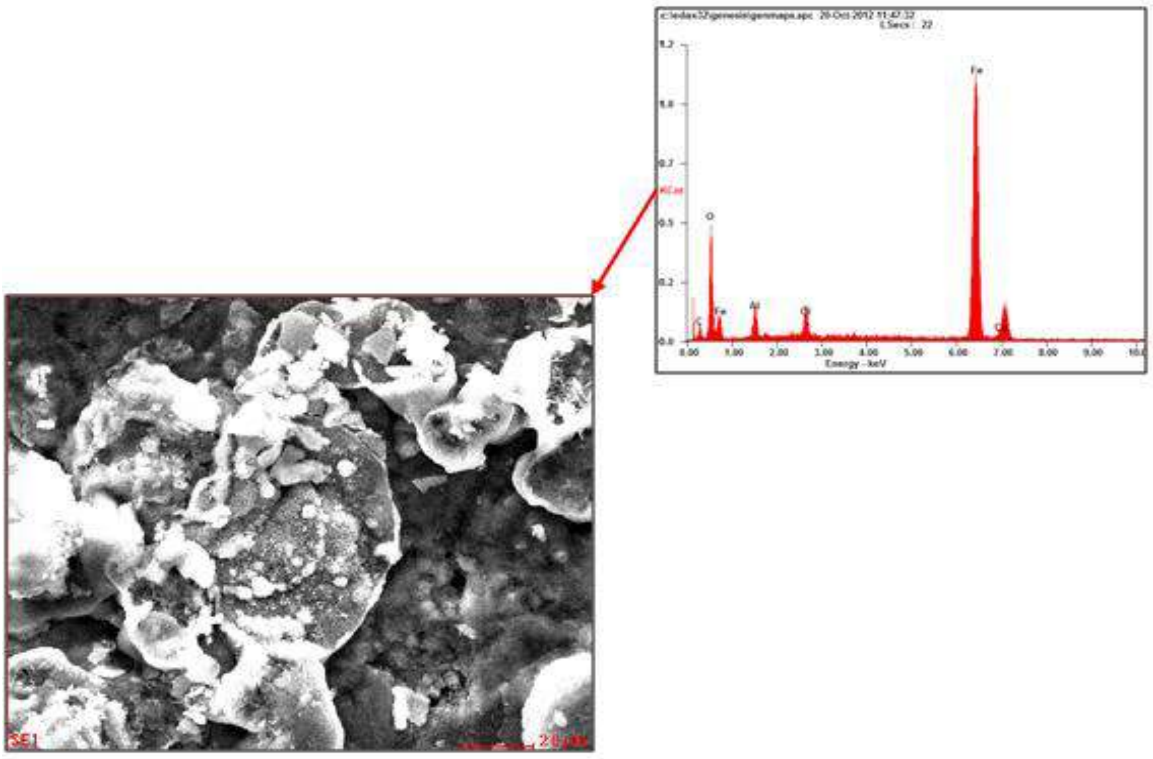

Fig. 9.25 SEM and EDAX of full frame view for specimen 10AFe1.0Co1100(1) after corrosion in 1N HCl at 2000X magnification

The present specimen shows the highest anti-corrosive efficiency along with the presence of nano size particles of aluminium chlorate and cobalt chlorate phases respectively. Therefore, the full frame the EDAX of specimen at 2000X and at 20000X was recorded along with regional EDAX of specimen at 2000X. Fig. 9.25 shows the SEM image of Fig. 9.24(b) along with full frame EDAX pattern. The corresponding elemental profile of the specimen is shown in Table 9.6. Various constituents present include carbon (C), oxygen (O), aluminium (Al), chlorine (Cl), iron (Fe) and cobalt (Co). In the present full frame selection carbon is 16.23 wt%, oxygen is 26.33 wt%, aluminium is 04.63 wt%, chlorine is 02.25 wt%, iron is 49.36 wt% and cobalt is 01.20 wt%. Atomic fraction of cobalt oxide was found to be almost same as in the starting composition. Fig. 9.26 shows the SEM image of Fig. 9.24(d) along with full frame EDAX pattern of specimen 10AFe1.0Co1100(1) showing nano size particles after corrosion in 1N HCl. Corresponding elemental profile is given in Table 9.6.

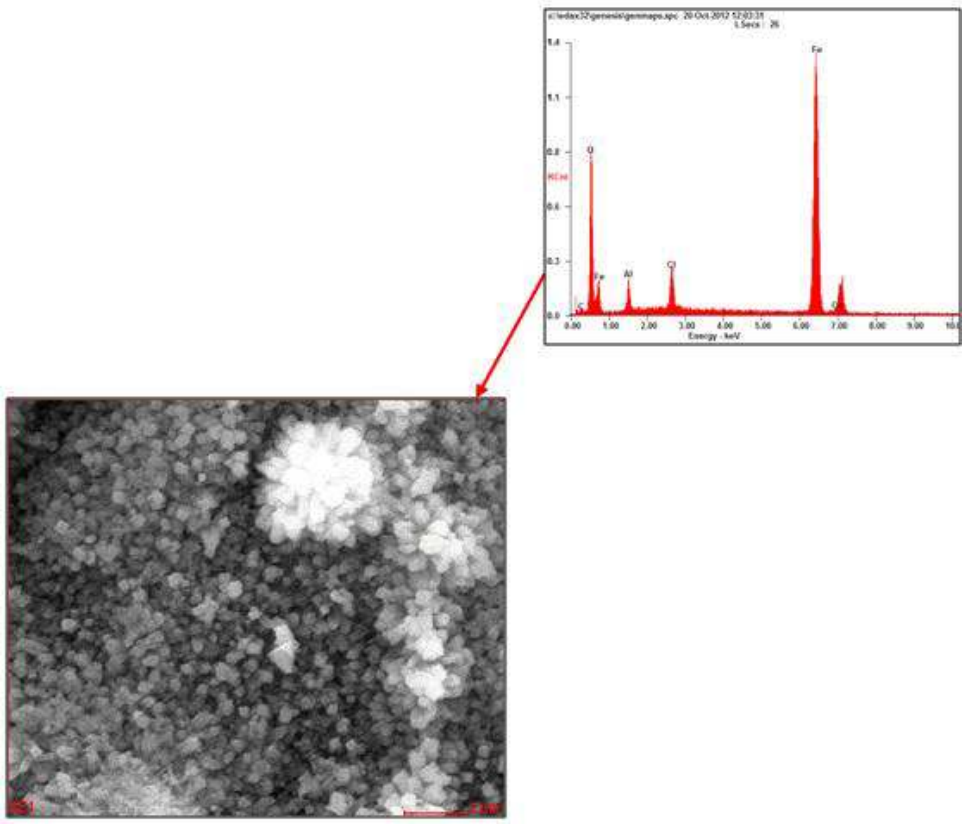

Fig. 9.26 SEM and EDAX of full frame of the specimen 10AFe1.0Co1100(1) showing nano size particles after corrosion in 1N HCl at 20000X magnification

The present view shows the presence of carbon (C), oxygen (O), aluminium (Al), chlorine (Cl), iron (Fe) and cobalt (Co) respectively. In the present full frame selection carbon is 05.73 wt%, oxygen is 34.26 wt%, aluminium is 04.88 wt%, chlorine is 03.95 wt%, iron is 50.46 wt% and cobalt is 00.73 wt%. It is seen in the present result that there is formation of smaller nano size particles of various constituents present in the nanocomposite specimen. Atomic fractions of various elements indicate the presence of nano size particles of aluminium chlorate and cobalt chlorate. Atomic fraction of iron and aluminium was almost found to be same in Fig. 9.25 and 9.26. Cobalt oxide concentration was more in Fig. 9.25 in comparison to Fig. 9.26. Thus, it can be concluded from the above discussion that due to the formation of nano aluminium chlorate and cobalt chlorate phases, a passivating film is formed on the specimen surface which reduces the corrosion of the nanocomposite specimens.

Table 9.6 Elemental Profile of full frame 10AFe1.0Co1100(1) specimen after corrosion

Composition	Full Frame of Fig. 9.25		Full Frame of Fig. 9.26	
	Wt%	At%	Wt%	At%
C	16.23	32.68	05.73	12.47
O	26.33	39.78	34.26	55.96
Al	04.63	04.15	04.88	04.73
Cl	02.25	01.53	03.95	02.91
Fe	49.36	21.37	50.46	23.61
Co	01.20	00.49	00.73	00.32

After EDAX study of full frame microstructure of specimen 10AFe1.0Co1100(1) (Fig. 9.24(b)) it was worthwhile to find out elemental profile of different regions of the microstructures. Fig. 9.27 shows the SEM image of Fig. 9.24(b) and EDAX patterns of different regions (a, b, and c) of microstructure. Table 9.7 reports its elemental profile. EDAX was recorded at 3 regions. Region “a” corresponds to nano particle region; “b” corresponds to iron region and “c” shows a single nano particle within region “a”. The specimen shows the presence of carbon (C), oxygen (O), aluminium (Al), chlorine (Cl), iron (Fe) and cobalt (Co) respectively.

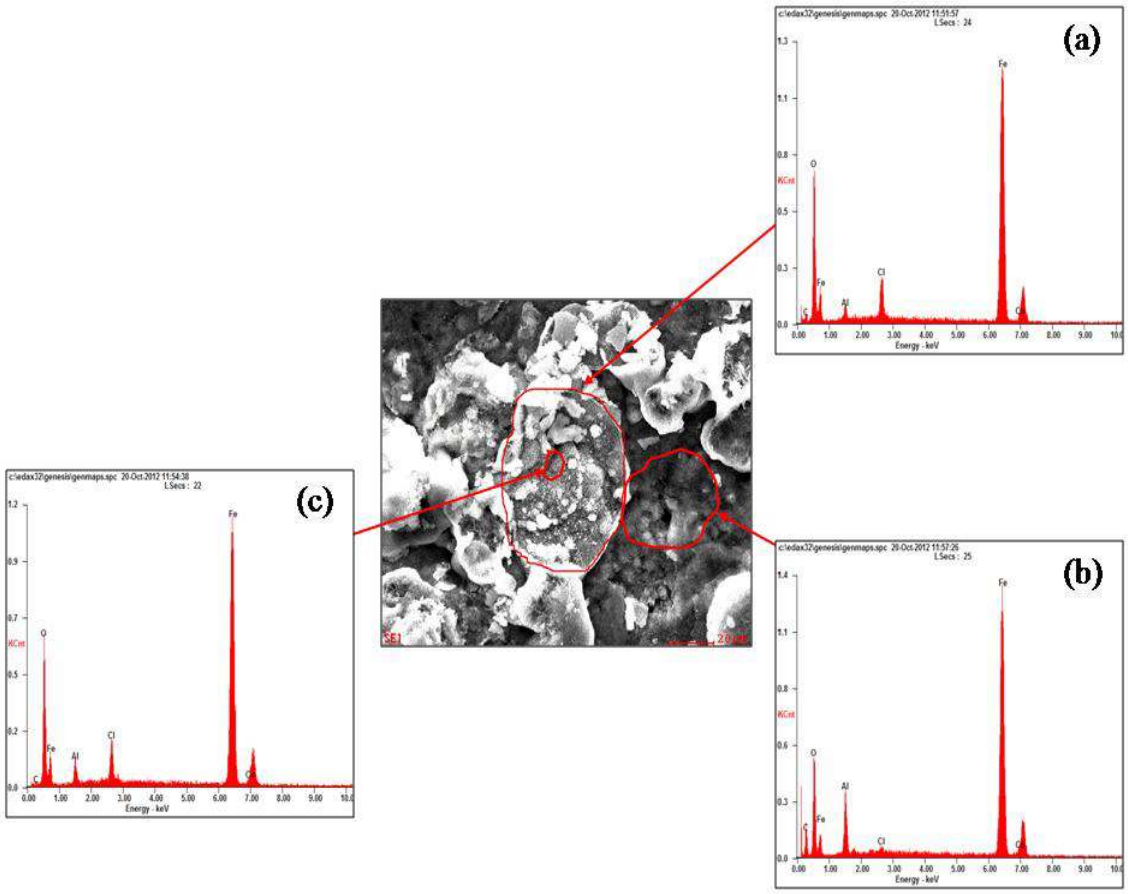

Fig. 9.27 SEM and EDAX of different regions (a, b, and c) for specimen 10AFe1.0Co1100(1) after corrosion in 1N HCl at 2000X magnification

Table 9.7 Elemental Profile of various constituents of 10AFe1.0Co1100(1) specimen after corrosion

Composition	a		b		c	
	Wt%	At%	Wt%	At%	Wt%	At%
C	07.11	15.62	25.54	45.55	04.08	09.51
O	32.41	53.41	23.93	32.05	31.15	54.57
Al	02.62	02.56	07.11	05.64	04.27	04.43
Cl	04.09	03.04	00.49	00.30	04.00	03.16
Fe	53.17	25.10	42.31	16.23	55.67	27.93
Co	00.60	00.27	00.62	00.23	00.83	00.39

Region “a” shows 07.11 wt% of carbon, 32.41 wt% of oxygen, 02.62 wt% of aluminium, 04.09 wt% of chlorine, 53.17 wt% of iron and 00.60 wt% of cobalt.

Region “b” shows 25.54 wt% of carbon, 23.93 wt% of oxygen, 07.11 wt% of aluminium, 00.49 wt% of chlorine, 42.31 wt% of iron and 00.62 wt% of cobalt. Region “c” shows 04.08 wt% of carbon, 31.15 wt% of oxygen, 04.27 wt% of aluminium, 04.00 wt% of chlorine, 55.67 wt% of iron and 00.83 wt% of cobalt. It can be concluded on the basis of the above result that there is a presence of all the constituent elements in the present micrograph. Atomic fraction of iron is high in region “a” and “c” whereas it is less in “b”. Atomic fraction of cobalt was found to be equal in all the three regions. Atomic fraction of aluminium was found to be high in “b” as compared to “a” and “c”. Expected compound formed in region “a” is aluminium chlorate ($AlCl_3O_{12}$) with trace amount of cobalt chlorate ($CoCl_2$).

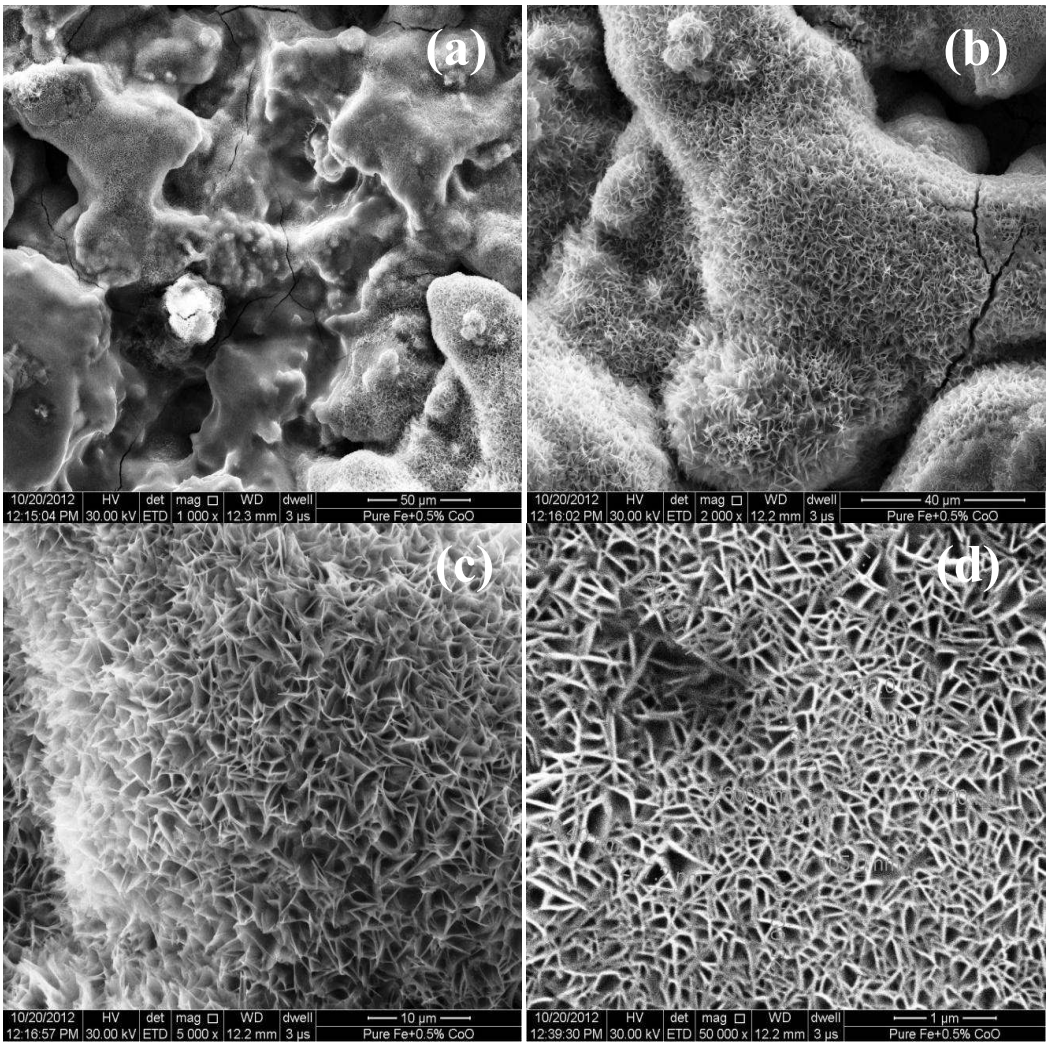

Fig. 9.28 SEM of pure iron specimen with 0.5% CoO after corrosion in 1N HCl at (a) 1000X (b) 2000X (c) 5000X and (d) 50000X magnification respectively

Fig. 9.28 shows the SEM of pure iron specimen with 0.5% CoO after corrosion in 1N HCl at (a) 1000X (b) 2000X (c) 5000X and (d) 50000X magnification respectively. SEM micrograph at 1000X magnification (Fig. 9.28(a)) shows the flower type distribution of the particles. The same micrograph when viewed at 2000X (Fig. 9.28(b)) shows more distinct view of the present phases. Fig. 9.28(c) shows the micron and sub micron size rods of the formed compound. Fig. 9.28(d) shows the nano size rods of the phase formed after the corrosion phenomenon on the surface of the specimen. Anti-corrosion efficiency of the present specimen is similar to the specimen 10AFe1.0Co1100(1) and was found to be better in comparison with the pure iron and 10AFe0.5Co1100(1).

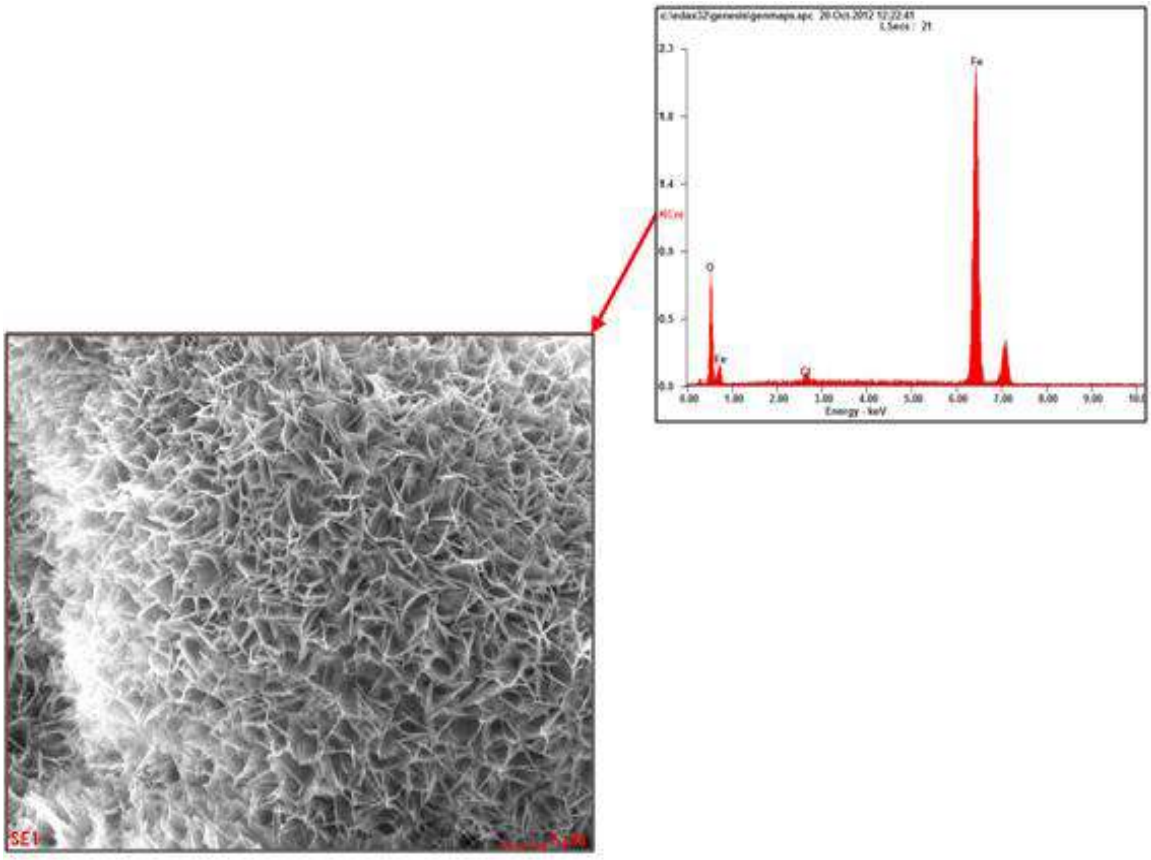

Fig. 9.29 SEM and EDAX of full frame of pure iron specimen with 0.5% CoO after corrosion in 1N HCl at 5000X magnification

Fig. 9.29 shows the SEM image of Fig. 9.28(c) along with full frame EDAX. The corresponding elemental profile of the specimen surface is given in Table 9.8 respectively. The results showed the presence of three elements namely oxygen (O), chlorine (Cl) and iron (Fe). The weight percent presence of three elements was found to be oxygen 23.20 wt%, chlorine 01.18 wt% and iron 75.63 wt% respectively. Atomic fraction of iron was found to be highest followed by oxygen and chlorine. It was found from this analysis that there is a formation of nano size iron chloride ($FeCl_2$) phase on the surface of the specimen.

Table 9.8 Elemental profile of full frame pure iron specimen with 0.5% CoO specimen after corrosion

Composition	Full Frame	
	Wt%	At%
O	23.20	51.11
Cl	01.18	01.17
Fe	75.63	47.73

9.4 Corrosion Behavior of CeO_2 Doped Fe-Al_2O_3 Metal Matrix Nanocomposites

Powders of electrolytic grade iron metal (99.5% purity and particle size 250-300 mesh (49-58 μm)) and active aluminum oxide (particle size 70-230 mesh (63-210μm)) and cerium oxide (99.9 % purity) were used as starting materials. Composition of the composite was 90% Fe and 10% Al_2O_3 by weight. 0.5 and 1.0% by weight of the cerium oxide was added as a dopant in this nanocomposite system. Appropriate mixtures of Fe, Al_2O_3, CeO_2 and binder were dry ball milled for 2 hours using zirconia balls as the grinding and mixing media with powder to ball ratio as 1:2. Cylindrical compacts were sintered in an argon atmosphere at 1100°C for 1h. A nomenclature e.g. 10AFe0.5Ce1100(1) is given to each specimen. Here A denotes the aluminum oxide, Fe denotes iron, 0.5Ce denotes the percentage of cerium oxide, 1100 denotes the sintering temperature, 1denotes time of sintering in hr. The specimens for the corrosion measurement were cut with 12 mm diameter and 2 mm height.

9.4.1 Tafel Polarization and Corrosion Behavior

The tafel polarization curves for pure iron specimen and three different specimens containing fixed amount of aluminium oxide (Al_2O_3) and varying amount of cerium oxide (CeO_2) in 1N HCl solution are shown in Fig. 9.30.

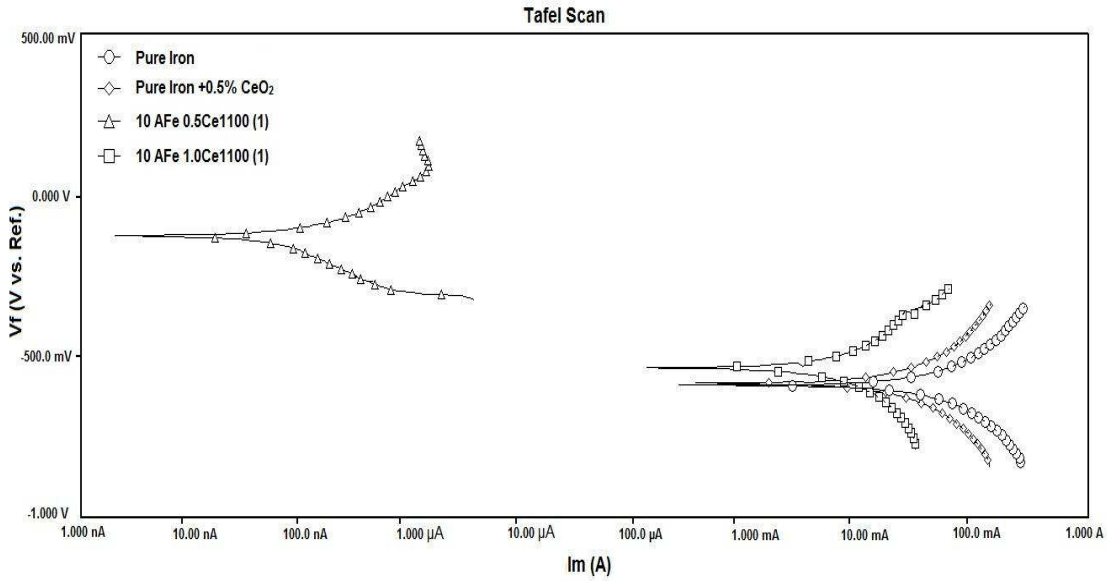

Fig. 9.30 Tafel Polarization plots of cerium oxide doped specimens

The electrochemical parameters such as corrosion potential (E_{corr}), corrosion rate (C_r), corrosion current density (I_{corr}) and anti-corrosive efficiency (μ_p) obtained from tafel polarization curves are given in Table 9.9. The values of corrosion potential (E_{corr}), corrosion current density (I_{corr}), were evaluated from anodic and cathodic regions of Tafel plots. The linear segments of anodic and cathodic curves were extrapolated to corrosion potential to obtain corrosion current densities (I_{corr}). Anti-corrosion efficiency (μ_p %) was evaluated from the measured I_{corr} values using the relationship:

$$\mu_p\ \% = (I^o_{corr} - I^i_{corr}) / I^o_{corr} * 100$$

where I^o_{corr} and I^i_{corr} are values of corrosion current density for pure iron and for specimens with aluminium oxide and cobalt oxide as reinforcement respectively.

Table 9.9 E_{corr}, Corrosion rate, I_{corr} and anti-corrosive efficiency (μ_p) values for the various CeO_2 doped specimens

Sl. No.	Sample Code	E_{corr} (mV)	I_{corr} (µA)	Corrosion rate (mpy)	μ_p (%)
1.	Pure Fe	-559	200000	92,080	-
2.	Pure Fe+0.5% CeO_2	-549	127000	81,000	36.50
3.	10AFe0.5Ce1100(1)	-129	0.329	0.0813	99.99
4.	10AFe1.0Ce1100(1)	-535	74300	18,390	62.85

It is observed from these results (Fig. 9.31 and Table 9.11) that the corrosion rate for the Pure Fe specimen [92080 mpy] is highest followed by Pure Fe+0.5% CeO_2 [81000 mpy]. Specimen Pure Fe and Pure Fe+0.5% CeO_2 showed corrosion potential value of -559 mV and -549 mV whereas corrosion current value of the specimen Pure Fe and Pure Fe+0.5% CeO_2, was found to be 200000 µA and 127000 µA. Specimen 10AFe1.0Ce1100(1) showed corrosion rate of 18,390 mpy whereas specimen 10AFe0.5Ce1100(1) showed corrosion rate of 0.0813 mpy. Corrosion potential of 10AFe0.5Ce1100(1) and 10AFe1.0Ce1100(1) was found to be -129 mV and -535 mV. It is also observed from the results that corrosion potential (E_{corr}) for the synthesized specimens varied from -559 to -129 mV. Specimen 10AFe0.5Ce1100(1) shows highest shift of E_{corr} (430 mV) towards noble direction followed by 10AFe1.0Ce1100(1). Corrosion current of the specimen 10AFe0.5Ce1100(1) and 10AFe1.0Ce1100(1) was found to be 0.329 µA and 74300 µA respectively. Further, the variation of corrosion rate of these specimens can be explained on the basis of the compositions of these specimens. It was seen that by the addition of 0.5% CeO_2 in pure iron, the anti-corrosion efficiency was found to be 36.50%. For specimen 10AFe0.5Ce1100(1) further addition of 10% Al_2O_3 and 0.5% CeO_2 in iron matrix gives 99.99% anti-corrosion efficiency. Addition of 1.0% CeO_2 nanocomposite specimen (90% Fe + 10% Al_2O_3) showed 62.85% anti-corrosion efficiency. It is interesting to note that corrosion rate for specimen 10AFe0.5Ce1100(1) is minimal

i.e. 0.0813 mpy. The superior corrosion resistance of specimen 10AFe0.5Ce1100(1) and 10AFe1.0Ce1100(1) can be attributed to the existence of nano size particles of Al_2O_3 and CeO_2 which instantly undergoes passivation forming passive film on the iron surface which protects the corrosion of iron in HCl solution. Similar results for the formation of passivation film due to the presence of chromium in the stainless steel reported by Song (2005). Gupta and Birbilis (2015) also reported the presence of a passivation film while studying the corrosion behavior of chromium containing nano crystalline stainless steel. Our results of CoO doped Fe- Al_2O_3 metal matrix nancomposites are in accordance with the results of Song (2005) as well as Gupta and Birbilis (2015). It was also seen from these results that the corrosion behavior of the specimen has generated finer nano size particles and nano size rods structure on the specimen surface. Further it is also observed that the presence of the nano size particles of cerium oxide particles has reduced the corrosion behavior to a significant level. The best corrosion characteristics was exhibited by the specimen 10AFe0.5Ce1100(1).

9.4.2 Phase and Microstructure

Fig. 9.31 shows XRD pattern of the corroded surfaces of (a) 10AFe0.5Ce1100(1) (b) 10AFe1.0Ce1100(1) and (c) Pure Fe+0.5% CeO_2 specimens respectively. Fig. 9.31(a) shows the XRD pattern of the specimen 10AF0.5Ce1100(1) which reveals the presence of iron and aluminum oxide. Fig. 9.31(b) shows the XRD pattern of the specimen 10AF1.0Ce1100(1) which reveals the presence of iron. Fig. 9.31(c) shows the XRD pattern of the specimen Pure Fe+0.5% CeO_2 which reveals no phase formation. From the above discussion it can be concluded that due to the corrosion action there is an amorphous layer formation on the specimen surface. The amorphous layer formation was less in the composite specimen where as it was more in the pure iron specimen.

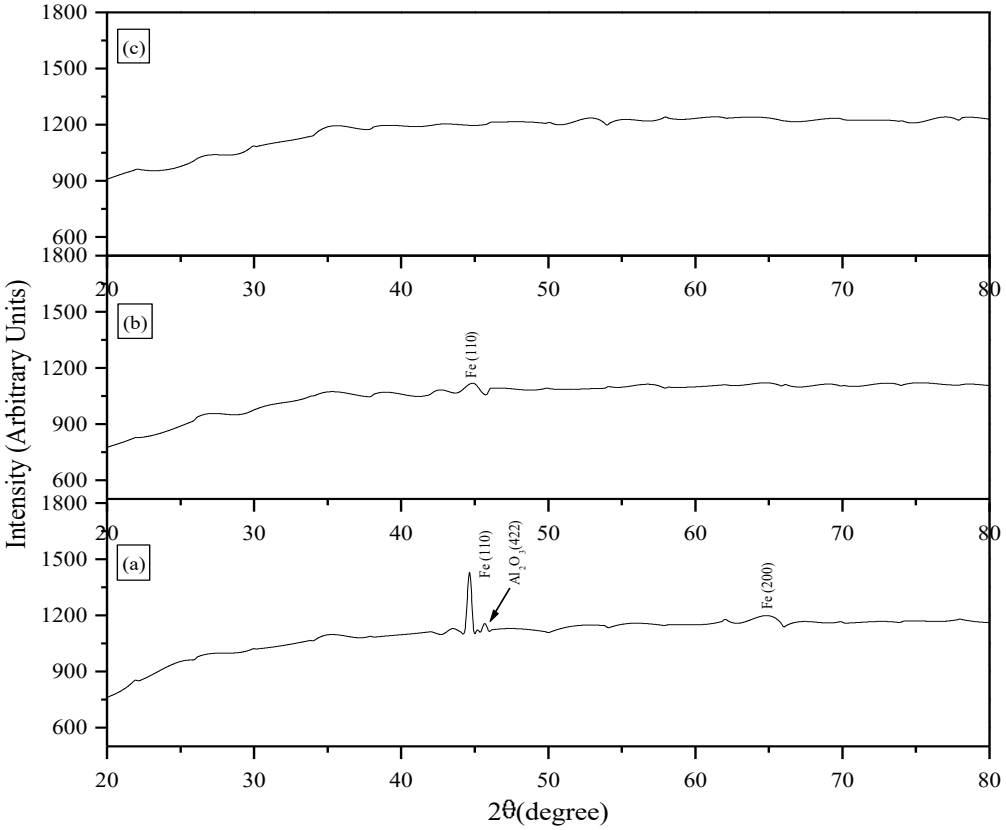

Fig. 9.31 XRD pattern of corroded surfaces of (a) 10AFe0.5Ce1100(1) (b) 10AFe1.0Ce1100(1) and (c) Pure Fe+0.5% CeO_2 specimens respectively

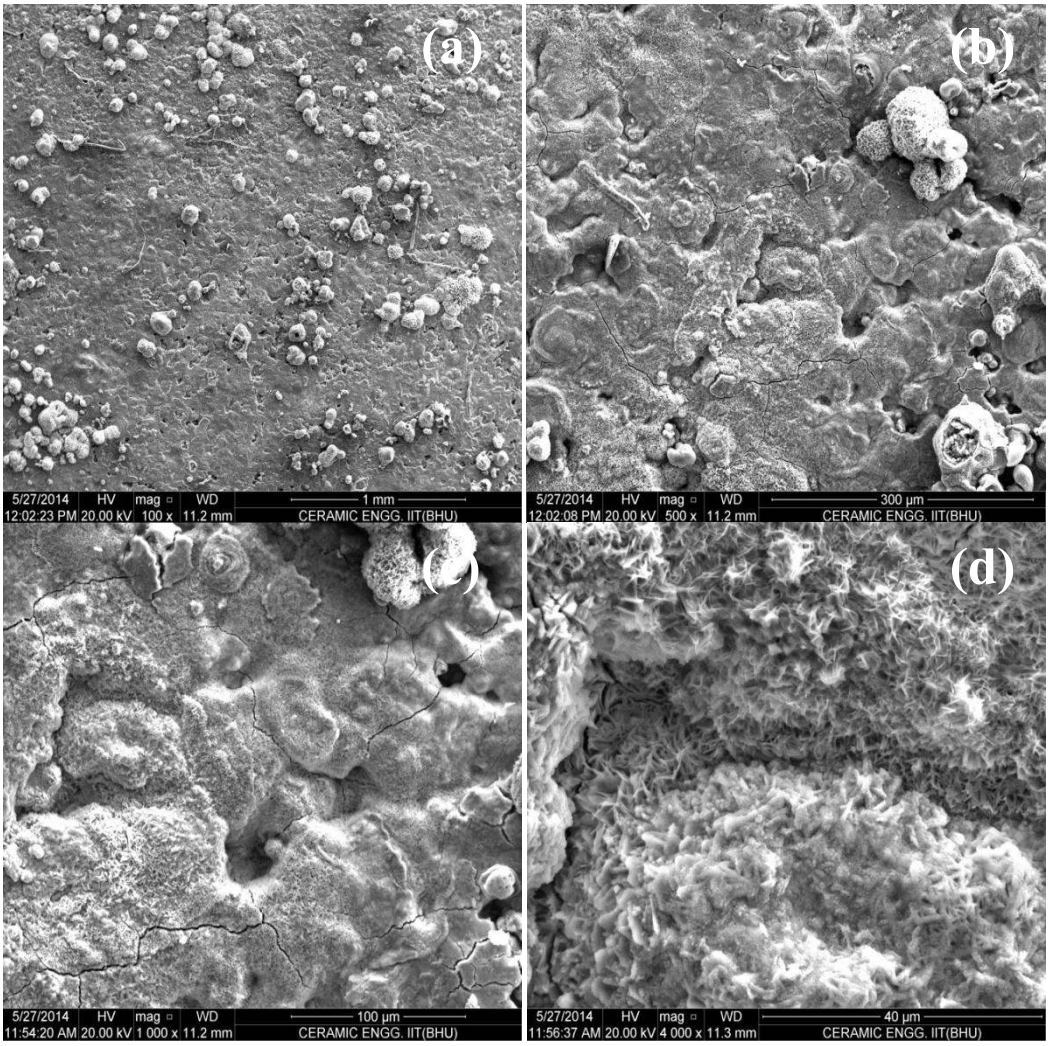

Fig. 9.32 SEM of specimen Pure Fe+0.5% CeO_2 after corrosion in 1N HCl at (a) 100X (b) 500X (c) 1000X and (d) 4000X magnification respectively

Fig. 9.32 shows the SEM of specimen Pure Fe+0.5% CeO_2 after corrosion in 1N HCl at (a) 100X (b) 500X (c) 1000X and (d) 4000X magnification respectively. Fig. 9.32 (a) shows the micrograph of the specimen at 100X revealing the highly dense and uniformly distributed grains of the specimen. Some grains are found separate which are of cerium oxide. Fig. 9.32 (b) shows the micrograph of the specimen at 500X which shows the uniform settled grains of the composite system along with that some grains of cerium oxide. These cerium oxide particles act as a protective layer on the composite specimen. During the corrosion action the cerium oxide particles which are present in the pores of the specimen come up to the surface to act as the protective

layer. Fig. 9.32 (c) and (d) shows the micrograph of the specimen at 1000X and 4000X which reveal the nano rod formation on the specimen surface. On an overall basis, it can be concluded that the presence of only 0.5% cerium oxide particles in pure iron specimen, increases the anti-corrosion efficiency by marginal level.

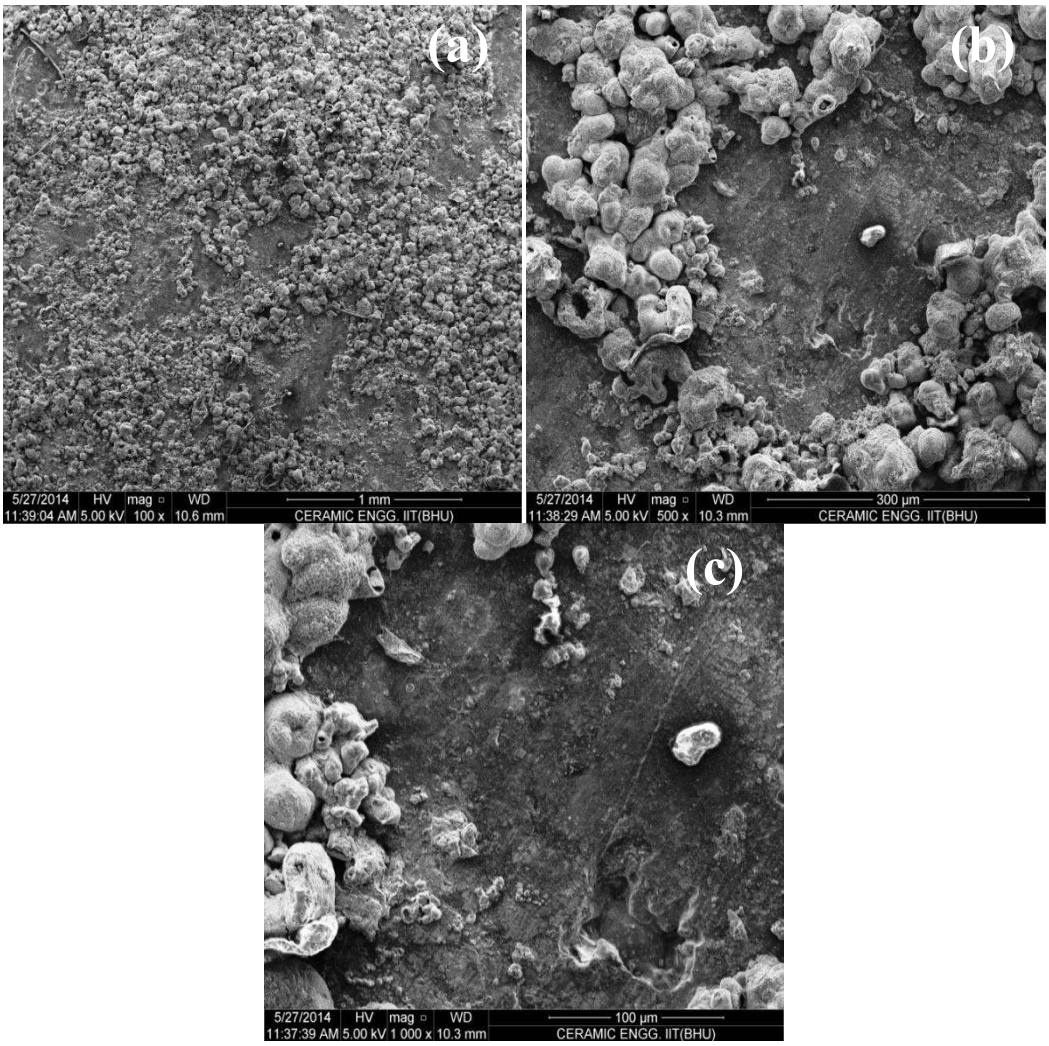

Fig. 9.33 SEM of specimen 10AFe0.5Ce1100(1) after corrosion in 1N HCl at (a) 100X (b) 500X and (c) 1000X magnification respectively

Fig. 9.33 shows the SEM of the specimen 10AFe0.5Ce1100(1) after corrosion in 1N HCl at (a) 100X (b) 500X and (c) 1000X magnification respectively. Fig. 9.33 (a) shows the micrograph of the specimen at 100X which shows the highly dense and uniformly distributed grains of the nanocomposite specimen. Some grains are found

separately which are of cerium oxide. Fig. 9.33 (b) shows the micrograph of the specimen at 500X which shows the uniform settled grains of the composite system along with some grains of cerium oxide. These cerium oxide particles act as a protective layer on the composite specimen. Fig. 9.33 (c) shows the micrograph of the specimen at 1000X which reveal the highly uniform and dense phase composite structure which remain undistorted even by the attack of 1N HCl. It can be seen in the present figure that a protecting layer of cerium oxide is formed on the surface and there is no pit formation on the nanocomposite specimen.

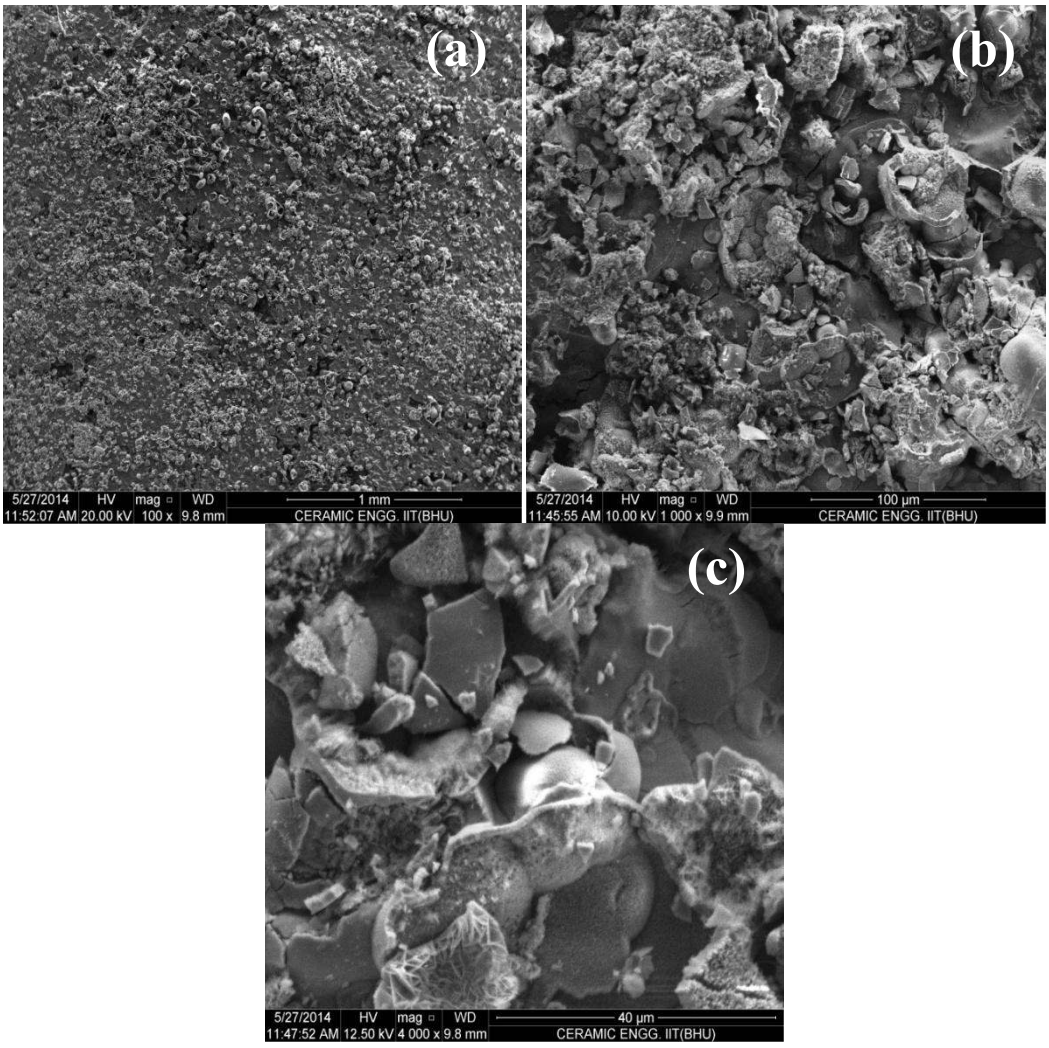

Fig. 9.34 SEM of specimen 10AFe1.0Ce1100(1) after corrosion in 1N HCl at (a) 100X (b) 1000X and (c) 4000X magnification respectively

Fig. 9.34 shows the SEM of the specimen 10AFe1.0Ce1100(1) after corrosion in 1N HCl at (a) 100X (b) 1000X and (c) 4000X magnification respectively. Fig. 9.34 (a) shows the micrograph of the specimen at 100X revealing highly densified and uniformly distributed grains of the nanocomposite specimen. Some grains are found separate which are of cerium oxide. The amount of the cerium oxide is more in the present system as compared to the previous specimen. Fig. 9.34(b) shows the micrograph of the specimen at 1000X which shows the uniform settled grains of the composite system along with that some grains of cerium oxide are also present. These cerium oxide particles act as a protective layer on the composite specimen. During the corrosion action the cerium oxide particles which are present in the pores of the specimen come up to the surface to act as the protective layer. Fig. 9.34 (c) shows the micrograph of the specimen at 4000X which reveals the nano rod formation on the specimen surface.

On an overall basis it can be concluded that in Fe-Al_2O_3 metal matrix nanocomposites all the corrosion reactions are electrochemical in nature. At anodic sites on the surface of the nanocomposite iron goes into solution as ferrous ions. It constitutes the anodic reaction. In Fe-Al_2O_3 metal matrix nanocomposites, a nano iron aluminate phase is formed in which iron atoms undergo oxidation to ions, they release electrons whose negative charge would quickly build up in the metal and prevent further anodic reaction, or corrosion. Thus, this dissolution will only continue if the electrons released can pass to a site on the metal surface where a cathodic reaction is possible. At a cathodic site the electrons react with some reducible component of the electrolyte and are themselves removed from the metal. This reducible compound when react with some ceramic material such as Al_2O_3 or CoO leads to the formation of aluminium chlorate ($AlCl_3O_{12}$) or cobalt chlorate ($CoCl_2$) phases respectively. The rates of the anodic and cathodic reactions must be equivalent according to Faraday's Laws which is being determined by the total flow of electrons from anodes to cathodes known as the "corrosion current", I_{corr}. Since the corrosion current must also flow through the electrolyte by ionic conduction the conductivity of the electrolyte will influence the way in which corrosion cells operate. The corroding

piece of metal is described as a "mixed electrode" since simultaneous anodic and cathodic reactions are proceeding on its surface. The mixed electrode is a complete electrochemical cell on one metal surface.

The most common and important electrochemical reactions in the corrosion of iron are thus

Anodic reaction (corrosion)

$$Fe \rightarrow Fe^{2+} + 2e \tag{9.1}$$

Cathodic reaction (simplified)

$$2H^{+} + 2e \rightarrow H_2 \tag{9.2}$$

$$H_2O + \frac{1}{2}O_2 + 2e \rightarrow 2OH^{-} \tag{9.3}$$

Reaction given in equation 9.2 is most common in HCl containing acids and the most important reaction is oxygen reduction eq. 9.3. In the latter case corrosion is usually accompanied by the formation of solid corrosion debris from the reaction between the anodic and cathodic products.

$$Fe^{2+} + 2OH^{-} \rightarrow Fe(OH)_2 \text{ , iron (II) hydroxide} \tag{9.4}$$

Pure iron (II) hydroxide is white but the material initially produced by corrosion is normally a greenish colour due to partial oxidation in air.

$$2Fe(OH)_2 + H_2O + \frac{1}{2}O_2 \rightarrow 2Fe(OH)_3 \text{ , hydrated iron (III) oxide} \tag{9.5}$$

Further hydration and oxidation reactions occur which eventually forms a complex mixture whose exact constitution will depend on other trace elements present. Because the film of rust is precipitated as a result of secondary reactions it is porous and absorbent and tends to act as a sort of harmful poultice which encourages further corrosion. For other metals or different environments different types of anodic and

cathodic reactions may occur. If solid corrosion products in the form film are produced directly on the surface as the first result of anodic oxidation these may provide a highly protective nano particle/rod on surface which retards further corrosion, the surface is then said to be “passive” [Lei et al. (2012)].

Further it was also observed in the present case that the corrosion behavior of the metal matrix nanocomposites is improved due to the following reasons:

1) During corrosion in Fe- (5%/10%) Al_2O_3 metal matrix nanocomposite system carried out in freely aerated 1N HCl solution leads to the formation of aluminium chlorate ($AlCl_3O_{12}$) phase. Aluminium chlorate phase forms a film on the surface of the specimen due to the chemical reaction of alumina with hydrochloric acid. Formation of aluminium chlorate film is in nano size.

2) CoO doped Fe-Al_2O_3 metal matrix nanocomposite system showed the formation of nano size film of aluminium chlorate ($AlCl_3O_{12}$) and cobalt chlorate ($CoCl_2$). Due to the chemical reaction between cobalt oxide and hydrochloric acid a cobalt chlorate phase forms whereas aluminium chlorate forms due to the chemical reaction between alumina and hydrochloric acid. Finer nano size particles of aluminium chlorate are found after the corrosion. Specimen 10AFe1.0Co1100(1) and Pure Fe+0.5% CoO showed the highest corrosion protection.

3) CeO_2 doped Fe-Al_2O_3 metal matrix nanocomposite system showed the formation of nano amorphous layer on the specimen surface. Specimen 10AFe0.5Ce1100(1) showed the highest anti-corrosion efficiency with the presence of protective layer of cerium oxide particles on the surface of the specimen.